THE ASTROPHYSICAL JOURNAL, 400:410–429, 1992 December 1

A SPATIAL, KINEMATICAL, AND DYNAMICAL ANALYSIS OF ABELL 400

TIMOTHY C. BEERS[1,2] AND KARL GEBHARDT
Department of Physics and Astronomy, Michigan State University, East Lansing, MI 48824

JOHN P. HUCHRA,[1] WILLIAM FORMAN, AND CHRISTINE JONES
Harvard/Smithsonian Center for Astrophysics, 60 Garden Street, Cambridge, MA 02138

AND

GREGORY D. BOTHUN[2]
Department of Physics and Astronomy, University of Oregon, Eugene, OR 97403
Received 1992 April 20; accepted 1992 June 6

ABSTRACT

A detailed spatial, kinematical, and dynamical analysis is presented for the cluster A400, based on a nearly complete redshift survey of bright galaxies within 1 Mpc of the cluster center (88 of 92 galaxies in the field studied by Dressler). The structure of this cluster is shown to be rather complex. We identify a dispersed component with a high fraction of spiral galaxies at a velocity of 8200 km s^{-1}, and a background group with a mean velocity of 13,400 km s^{-1}. Although we consider a model in which A400 is comprised of a single cluster at a central location in velocity space on the order of 7000 km s^{-1}, we propose that the main body of A400 is composed of at least two individual subclusters.

If subclustering is ignored, the derived dispersion of the 88 galaxies with measured velocities within 4000 km s^{-1} of the bright dumbbell galaxy near the cluster center is 702 km s^{-1}. When kinematic information is used to split A400 into likely subclusters, the velocity dispersions of the individual units which make up this cluster are on the order of 200–300 km s^{-1}. If A400 is considered a single entity (including the dispersed high-velocity spiral-rich component), the inferred blue mass-to-light ratio is 1210 $M_\odot/L_\odot$. If the cluster at 7000 km s^{-1} is taken to be a single entity, the inferred mass-to-light ratio is 615 $M_\odot/L_\odot$, which is still higher than is found for most rich clusters. If the primary sublusters which make up this low-velocity structure are considered separately, their derived mass-to-light ratios drop to roughly 300 $M_\odot/L_\odot$, in line with estimates for other groups and clusters.

Application of a simple two-body dynamical model indicates that the two primary subclusters in A400 are bound to one another, and are presently infalling with relative velocity difference on the order of either 700 km s^{-1} or 2000 km s^{-1} depending on the projection angle of the system with respect to the plane of the sky. We argue that A400 is an example of a presently occurring merger, and that the individual components of the dumbbell galaxy were once individual D galaxies within the premerger subclusters.

A400 harbors the unusual radio source 3C 75, which is associated with the bright central dumbbell galaxy. Each component of the dumbbell galaxy exhibits a twin radio jet; these jets bend in a common direction on the sky. The complex structure of 3C 75 might well be explained by our subcluster collision model. The *Einstein* X-ray image of A400 exhibits an apparent asymmetry in the central regions, with a major axis approximately aligned along a direction parallel to the initial bend of the wide-angle–tail radio sources. The inferred collisional velocity of the subclusters is large enough to cause the bending in the radio jets due to the motion of the D galaxies through the intracluster gas trapped in the potential wells of each subcluster.

Subject headings: galaxies: clustering — galaxies: distances and redshifts

1. INTRODUCTION

Primarily because it is relatively nearby, the cluster Abell 400 (Zw 415-41) has received considerable recent attention in the literature. This cluster, which Abell (1958) assigned to richness class 1, has a rather high fraction of galaxies (48%) classified as spirals or irregulars in the field studied by Dressler (1980). In his thesis, Bothun (1981) obtained a velocity dispersion for cluster members on the order of 500 km s^{-1}, but he noted a higher mean velocity for spirals in the outer region of the cluster. From a sample of 19 member galaxies with redshifts measured by an early multiple-fiber instrument, Hintzen et al. (1982) obtained a velocity dispersion of 345^{+79}_{-51} km s^{-1} and argue that the dispersion may be even lower owing to the possible presence of contamination from galaxies associated with the nearby Perseus-Pisces supercluster.

A400 is one of the primary clusters which Aaronson et al. (1986) use to map local deviations in the Hubble flow. These authors obtain Tully-Fisher distances for seven galaxies in the region of A400. Although there is no significant peculiar velocity (relative to the local Hubble flow) exhibited by A400, there is a lingering ambiguity over what value to use as the proper mean redshift in light of the multiple velocity components which are shown in this paper to be present in A400. In particular, the mean velocity of the galaxies with distance estimates is some 800 km s^{-1} higher than the mean found for all galaxies in this paper.

[1] Research reported herein is based partly on observations obtained at the Multiple Mirror Telescope, a joint facility of the Smithsonian Institution and the University of Arizona.

[2] Research reported herein is based in part on observations obtained with the Palomar 5 m Telescope, a facility of the California Institute of Technology.

A400 is one of the clusters which appeared to exhibit a double morphology in the maps of Geller & Beers (1982), although these authors did not claim statistical significance for the structure. A lack of significant substructure in A400 was also suggested in the study of West & Bothun (1990). Below we show that the apparent secondary clump to the northeast of the main structure is comprised of a superposition of a dispersed spiral-dominated component and a background group. A new map of the galaxy distribution based exclusively on kinematically selected members of A400 is shown below to be consistent with the cluster morphology seen in the *Einstein* X-ray map.

A400 is also of interest because it harbors a bright central "dumbbell" galaxy with nuclei separated by roughly 20 h^{-1} ($H_0 = 100\ h$ km s^{-1} Mpc^{-1}). Tonry (1985) discusses spectroscopic observations of the dumbbell galaxy, obtaining a relative velocity difference of 426 km s^{-1} between the two nuclei. In an investigation of the photometric properties of the dumbbell, Hoessel, Borne, & Schneider (1985) find no evidence for distortions in the isophotal structure of the dumbbell galaxy. In addition, these authors argue from the position of the individual nuclei in the Faber-Jackson diagram for other elliptical galaxies that the dumbbell is likely to be an example of two individual elliptical galaxies seen in projection. Contrary to this interpretation, Lauer (1988) considers the isophotal structure of the dumbbell galaxy in A400, and concludes that some sort of mutual interaction must be taking place.

Tremaine (1990) suggests that the existence of dumbbell galaxies may be indicative of a recent collision of two subclusters, each of which possessed a D/cD galaxy prior to the collision. In this scenario the violent relaxation process is incomplete, that is, the subclusters retain some "memory" of their individual premerger kinematic properties for a prolonged time after the merger is initiated. Below we show that the individual components of the dumbbell galaxy have velocities which are quite close to the central locations in velocity space of the galaxies in two individual subclusters identified from our redshift survey, lending credence to the Tremaine model.

The radio source associated with the dumbbell galaxy (3C 75) is rather complex. As discussed by Owen et al. (1985), both nuclei of this dumbbell galaxy host radio sources with extended twin jets which are observed to bend in a common direction (to the northeast). Below we show that the X-ray map of A400 obtained with the *Einstein Observatory* exhibits a central asymmetry, with a primary axis nearly coincident with the symmetry axis of the extended radio tails. This result, along the identification of a kinematic signal for the existence of at least two primary sublcusters, is strong circumstantial evidence for a collisional origin of the bending of the jets in 3C 75.

In the present paper we report 97 new redshift measurements for 83 galaxies within 3° (3.6 h^{-1} Mpc) of A400. When combined with previously reported samples, 109 velocities are now available for galaxies within 3° of A400. A total of 99 of these galaxies have velocities within 4000 km s^{-1} of the bright central dumbbell galaxy. In § 2 we discuss our new observations. In § 3 we discuss a kinematic analysis of the sample of galaxies within 1.5 h^{-1} Mpc of the cluster center, and a spatial and kinematic analysis of our nearly complete redshift survey of the galaxies within 1.0 h^{-1} Mpc of A400 listed by Dressler (1980). We apply an objective clustering algorithm, "partitioning around medoids" (PAM; Kaufman & Rousseeuw 1990), to asign galaxies from the Dressler sample to likely groups in velocity space. One of the groups we identify is spiral-rich (spiral fraction = 65%) and has a central location in velocity space some 1200 km s^{-1} higher than the remaining cluster galaxies. The majority of the spirals used by Aaronson et al. (1986) belong to this spiral-rich structure. A group of eight galaxies are identified at a velocity of roughly 13,400 km s^{-1}. The two remaining groups we identify are likely to be physical subclusters within A400. These subclusters are separated in radial velocities by 700 km s^{-1} from one another, and are dominated by elliptical and S0 galaxies (spiral fraction 35%–40%), but are nearly coincident on the plane of the sky. A new galaxy surface-density map is obtained from the galaxies kinematically identified as members of these subclusters.

In § 4 we consider the nature of A400 based on observations obtained with the imaging proportional counter (IPC) detector on the *Einstein Observatory*. From a simple hydrostatic, isothermal model we obtain an estimate of the total gravitational mass within 1.0 h^{-1} Mpc of the cluster center, $M_b = 7.2 \times 10^{13}\ h^{-1}\ M_\odot$, consistent with the summed mass of the subclusters we identify based on the optical data alone. We derive a new value for the spectroscopic beta parameter, $\beta_{\rm spec} = 0.59^{+0.32}_{-0.19}$, which is consistent with that obtained from a fit to the radially averaged X-ray surface brightness profile, $\beta_{\rm imag} = 0.57$.

In § 5 we obtain dynamical estimates of the masses and mass-to-light ratios of the cluster (when considered as a single entity) as well as for the individual subclusters. We discuss the application of simple two-body dynamical models (Beers, Geller, & Huchra 1982, hereafter BGH) to quantify the likely dynamical state of A400. In § 6 we summarize the evidence that A400 is presently undergoing a merger of two primary subclusters.

2. OBSERVATIONS

A host of telescopes were used to obtain the spectroscopic data reported in this paper. The bulk of our data (59 spectra of 45 galaxies) were obtained using the photon-counting Reticon system ("Z-machine"; Latham 1982) and the Cassegrain spectrograph on the Tillinghast 1.5 m telescope of the F. W. Whipple Observatory. A 600 line mm^{-1} grating was used to obtain a spectral resolution of 6–7 Å (FWHM) over the region 4500–7000 Å. Observations of four galaxies were obtained with a similar detector system in combination with a 300 line mm^{-1} grating on the Multipe Mirror Telescope (MMT) Cassegrain spectrograph. The resolution of the MMT observations is roughly 9 Å over the region 3500–7500 Å. Spectra of 31 galaxies were obtained with the 2D-Frutti detector system (Shectman 1984) and the double spectrograph on the Palomar Hale 5 m telescope. A 600 line mm^{-1} grating was used to obtain spectra with 4 Å resolution over the region 3500–5500 Å.

Optical redshifts were obtained by use of a cross-correlation procedure (Tonry & Davis 1979). Several different templates were employed, depending on the telescope/detector combination. For galaxies observed with the Tillinghast 1.5 m telescope, we used the extremely high-to-noise galaxy and stellar templates already in hand from the CfA redshift survey, yielding typical external velocity errors of less than 50 km s^{-1}. A moderate signal-to-noise template for the MMT spectra was constructed from summed spectra of globular clusters in M31. External errors in radial velocities measured with this setup on the MMT are in the range 30–60 km s^{-1}. Observations with the Hale 5 m telescope were cross-correlated with a template assembled from spectra of G9/K0 giant stars with known radial velocities (Abt & Biggs 1972) taken during the same

TABLE 1

POSITIONS AND VELOCITIES FOR GALAXIES IN THE REGION OF ABELL 400

Galaxy	3° ID	Right Ascension (1950)	Declination	Velocity (km s^{-1})	Error	Source	N	D80#	Group
(1)	(2)	(3)	(4)	(5)	(6)	(7)	(8)	(9)	(10)
0244+0711	1 B	02 44 36.0	+ 07 11 00	5430	150	5			
N 1095	2 B	02 45 00.0	+ 04 26 00	6364	32	T			
N 1011	3 B	02 45 42.0	+ 04 22 00	6207	26	T			
0245+0618	4 B	02 45 56.0	+ 06 18 49	8347	20	32-0			
0246+0619	5 B	02 46 00.0	+ 06 19 00	5959	20	6-17			
0250+0620	6 A	02 50 42.0	+ 06 20 00	5430	20	32-0			
0250+0338		02 50 48.0	+ 03 38 00	11409	28	T			
0251+0603A	7 A	02 51 03.0	+ 06 03 42	7386	20	32-0			
0251+0547	8 A	02 51 17.0	+ 05 47 06	7910	20	32-0			
0251+0603B	9 A	02 51 24.0	+ 06 03 00	7607	20	32-0			
0252+0524	10 A	02 52 23.0	+ 05 24 31	7406	80	H		9	a
0252+0558	11 A	02 52 36.0	+ 05 58 31	7604	34	T		70	a
0252+0552	12 A	02 52 40.9	+ 05 55 20	7495	20	T	2	62	a
				7455	20	32-0			
0253+0537	13 A	02 53 00.6	+ 05 37 25	6697	76	H		24	d
0253+0608	14 A	02 53 03.8	+ 06 08 49	6760	28	TZ		83	d
0253+0600	15 A	02 53 07.9	+ 06 00 57	8005	20	32-0		72	c
				8034	30	T			
0253+0617	16 A	02 53 18.6	+ 06 17 36	7709	20	32-0		85	a
0253+0610	17 A	02 53 27.8	+ 06 10 31	7696	31	MZ		82	a
0253+0554	18 A	02 53 34.1	+ 05 54 45	7895	100	S		61	c
0253+0545	19 A	02 53 39.0	+ 05 45 59	6284	62	MZ		34	d
0253+0419	20 B	02 53 40.0	+ 04 19 42	8267	20	32-0			
0253+0557	21 A	02 53 44.0	+ 05 57 15	7771	20	32-0		69	a
0253+0607	22 A	02 53 49.9	+ 06 07 02	7019	19	T	2	75	d
0253+0559	23 A	02 53 50.5	+ 05 59 38	7191	45	MZ		68	a
0254+0708	24 B	02 54 00.0	+ 07 08 00	8090	26	T			
0254+0542	25 A	02 54 01.9	+ 05 42 40	7115	20	T	2	33	a
0254+0547	26 A	02 54 03.5	+ 05 47 35	6954	42	H		48	d
0254+0447	27 A	02 54 06.0	+ 04 47 00	7724	24	TZ			
0254+0529	28 A	02 54 06.3	+ 05 29 18	7984	100	H		16	c
0254+0551	29 A	02 54 07.3	+ 05 51 14	7816	20	32-0		53	a
				7768	100	15-7			
0254+0540	30 A	02 54 13.9	+ 05 40 17	7448	27	T		27	a
0254+0601A	31 A	02 54 17.8	+ 06 00 18	6372	31	TZ		67	d
0254+0620	32 A	02 54 21.0	+ 06 20 00	8255	37	H		88	c
0254+0601B	33 A	02 54 23.4	+ 06 01 35	6767	38	MZ		71	d
0254+0543	34 A	02 54 26.8	+ 05 43 06	5791	50	H		32	d
0254+0507	35 A	02 54 31.1	+ 05 07 15	7453	22	T	2	3	a
0254+0546A	36 A	02 54 39.3	+ 05 46 47	7613	20	T	2	47	a
				7451	100	15-7			
0254+0554	37 A	02 54 41.2	+ 05 54 48	6808	100	15-7			
0254+0544	38 A	02 54 44.4	+ 05 44 46	6955	38	TZ		31	d
				6857	100	15-7			
0254+0546B	39 A	02 54 45.2	+ 05 46 54	6606	40	T		46	d
				6513	100	15-7			
0254+0556	40 A	02 54 47.2	+ 05 56 49	7495	100	15-7			
0254+0548	41 A	02 54 48.9	+ 05 48 46	6444	22	H		45	d
0254+0546C	42 A	02 54 55.2	+ 05 46 36	6842	17	T	2	44	d
				6870	100	15-7			
0254+0556	43 A	02 54 58.5	+ 05 56 39	7136	100	15-7		60	a
0254+0550	44 A	02 54 58.8	+ 05 50 48	7479	56	H		52	a
0254+0610	45 A	02 54 59.0	+ 06 10 58	8102	59	H		81	c
0254+0635	46 A	02 55 02.5	+ 06 35 47	6159	50	H		91	d
0255+0549A	47 A*	02 55 03.0	+ 05 49 38	6800	15	24		42	d
				6795	17	T	2		
				6752	100	15-7			
0255+0549B	48 A*	02 55 03.1	+ 05 49 20	7236	15	24		43	a
				7260	19	T	2		
0255+0531	49 A	02 55 03.9	+ 05 13 56	7561	33	T		6	a
0255+0539	50 A	02 55 04.8	+ 05 39 55	8089	100	15-7		26	c
0255+0622	51 A	02 55 05.4	+ 06 22 23	7386	29	H		87	a
0255+0528A	52 A	02 55 06.2	+ 05 28 18	7272	32	TZ		15	a
0255+0537A	53 A	02 55 06.5	+ 05 37 33	6634	100	15-7		23	d
0255+0546	54 A	02 55 07.1	+ 05 46 32	7079	100	15-7		40	a
0255+0545	55 A	02 55 07.4	+ 05 45 06	7200	100	S		30	a
0255+0547	56 A	02 55 08.4	+ 05 47 05	6665	100	15-7		39	d
0255+0549C	57 A	02 55 08.8	+ 05 49 39	7303	34	H		41	a
0255+0551	58 A	02 55 12.0	+ 05 51 09	6716	31	T		51	d
0255+0609	59 A	02 55 13.2	+ 06 09 37	7363	61	H		80	a
0255+0556	60 A	02 55 16.0	+ 05 56 20	5889	89	H		59	d
0255+0535	61 A	02 55 19.2	+ 05 35 13	6410	30	TZ		22	d
0255+0534	62 A	02 55 19.8	+ 05 34 58	6097	29	TZ		19	d
0255+0541	63 A	02 55 28.1	+ 05 44 18	6813	100	15-7			
0255+0538	64 A	02 55 33.0	+ 05 38 13	7348	23	TZ		21	a
				7248	100	15-7			
0255+0542	65 A	02 55 35.1	+ 05 42 17	7104	100	15-7		25	a

TABLE 1—*Continued*

Galaxy	3° ID	Right Ascension (1950)	Declination	Velocity (km s^{-1})	Error	Source	N	D80#	Group
(1)	(2)	(3)	(4)	(5)	(6)	(7)	(8)	(9)	(10)
0255+0546B	66 A	02 55 35.7	+ 05 46 21	6763	100	15-7		38	d
0255+0543	67 A	02 55 36.4	+ 05 43 01	6297	100	15-7		29	d
0255+0553	68 A	02 55 42.3	+ 05 53 42	6855	25	T		58	d
				6629	100	15-7			
0255+0634	69 A	02 55 45.8	+ 06 34 34	6243	39	H		89	d
0255+0600	70 A	02 55 49.9	+ 06 00 23	6576	33	T		66	d
0255+0606	71 A	02 55 50.9	+ 06 06 24	6708	20	32-0		74	d
				6744	31	T			
0255+0528B	72 A	02 55 52.0	+ 05 28 10	6974	52	H		14	d
0255+0521	73 A	02 55 54.7	+ 05 21 10	7410	70	H		8	a
0255+0558	74 A	02 55 59.1	+ 05 58 34	7383	33	T		65	a
0255+0613	75 A	02 56 05.7	+ 06 13 26	8384	100	H		84	c
0256+0524	76 A	02 56 10.0	+ 05 24 24	6848	47	H		10	d
0256+0609A		02 56 11.9	+ 06 09 59	13704	41	H		78a	b
0256+0609B		02 56 11.9	+ 06 09 59	13205	54	H		78b	b
0256+0610		02 56 12.2	+ 06 10 29	13521	35	T		77	b
0256+0557	77 A	02 56 14.8	+ 05 57 31	7430	40	T		64	a
0256+0555	78 A	02 56 15.7	+ 05 55 03	7190	24	T	2	57	a
0256+0559	79 A	02 56 16.5	+ 05 59 37	7930	46	T		63	c
0256+0609C		02 56 17.0	+ 06 09 15	13213	66	H		76	b
0256+0605	80 A	02 56 17.3	+ 06 05 14	6778	40	T		73	d
				6900	150	37			
0256+0604	81 A	02 56 22.1	+ 06 04 09	6790	31	T		92	d
0256+0547		02 56 25.3	+ 05 47 17	13223	32	TZ		37	b
0256+0556	82 A	02 56 37.3	+ 05 56 04	8125	100	S		56	c
0256+0706	83 B	02 56 38.0	+ 07 06 18	7628	20	32-0			
				7708	37	T			
0256+0550	84 A	02 56 42.2	+ 05 50 17	6839	23	H		50	d
0256+0549	85 A	02 56 46.9	+ 05 49 59	8205	20	32-0		49	c
0256+0608	86 A	02 56 55.6	+ 06 08 42	6809	21	T		79	d
0256+0553	87 A	02 56 56.9	+ 05 53 51	10226	112	H		54	c
0257+0514	88 A	02 57 01.5	+ 05 14 24	8269	44	H		5	c
0257+0513		02 57 03.2	+ 05 13 24	14441	52	H		4	b
0257+0533		02 57 04.4	+ 05 33 40	13273	82	H		18	b
0257+0544	89 A	02 57 07.6	+ 05 44 48	8340	33	H		28	c
0257+0532	90 A	02 57 10.1	+ 05 32 39	6824	40	H		17	d
0257+0547		02 57 10.5	+ 05 47 39	31118	100	H		36	e
0257+0530A		02 57 12.3	+ 05 30 09	13765	37	TZ		13	b
0257+0620	91 A	02 57 13.6	+ 06 20 06	8584	20	32-0		86	c
				8625	46	TZ			
0257+0546	92 A	02 57 21.4	+ 05 46 09	8480	45	H		35	c
0257+0634	93 A	02 57 21.7	+ 06 34 31	7307	41	TZ		90	a
0257+0536	94 A	02 57 30.2	+ 05 36 25	6652	15	T	4	20	d
0257+0530B	95 A	02 57 31.2	+ 05 30 48	8407	72	T		12	c
0257+0530C	96 A	02 57 42.1	+ 05 30 53	8618	15	T	3	11	c
0304+0405	97 B	03 00 41.0	+ 04 05 00	6932	20	32-0			
				6916	36	T			
0300+0418	98 B	03 00 42.0	+ 04 18 18	6003	20	32-0			
0302+0515	99 B	03 02 00.0	+ 05 15 00	8409	20	32-0			

SOURCE CODES.—H: Hale 5 m telescope. MZ: Multiple Mirror Telescope; also reported in Zabludoff, Huchra, & Geller 1990. S: Stauffer 1983, private communication. T: Tillinghast 1.5 m telescope. TZ: Tillinghast 1.5 m telescope; also reported in Zabludoff et al. 1990. 24: Tonry 1985. 6-17: Haynes & Giovanelli 1984. 15-7: Hintzen et al. 1982. 32-0: Bothun et al. 1985.

observing run. External errors in the derived radial velocities are typically 30–40 km s^{-1}.

In Table 1 we present the best available positions and velocities for galaxies with known redshifts and located within 3° of the cluster center. Only those galaxies with known velocities within ± 4000 km s^{-1} of the mean velocity of the bright dumbbell galaxy near the local density maximum of the cluster are assigned a 3° identification. (Individual components of the dumbbell are indicated by asterisks in the second column.) Galaxies with velocities which fall outside this range are reported in the table but do not have a 3° identification assigned to them. Those galaxies within 1.5 h^{-1} Mpc of the cluster center at the redshift distance of the dumbbell galaxy are assigned to sample A; those galaxies *outside* the 1.5 h^{-1} Mpc radial distance but *inside* the 3° circle are assigned to sample B.

For the majority of the galaxies with newly measured redshifts, we have obtained positions (accurate to roughly 2″–3″) with the two-axis Grant machine at Kitt Peak National Observatory or the two-axis measuring engine at the Center for Astrophysics. For galaxies in clusters studied by Dressler (1980), we list his coordinates (unless otherwise available from the two-axis machine measurements). Positions for galaxies with previously reported redshifts are taken from the original sources. If no better coordinate is available, we report the position listed in the Zwicky (Zwicky et al. 1961–1968) or Nilson (1973) catalogs.

Column (1) of Table 1 lists the galaxy name. Column (2) lists the identification number for the 3° sample. Columns (3) and (4) list the 1950 equatorial coordinates. In columns (5) and (6) we report each galaxy's heliocentric velocity (cz_h) and 68% (1 σ) measurement error. In column (7) we list the source of the spectroscopic observation. For previously published data, the numerical codes are those assigned in Huchra (1990). Several galaxies have more than one available spectrum. We indicate

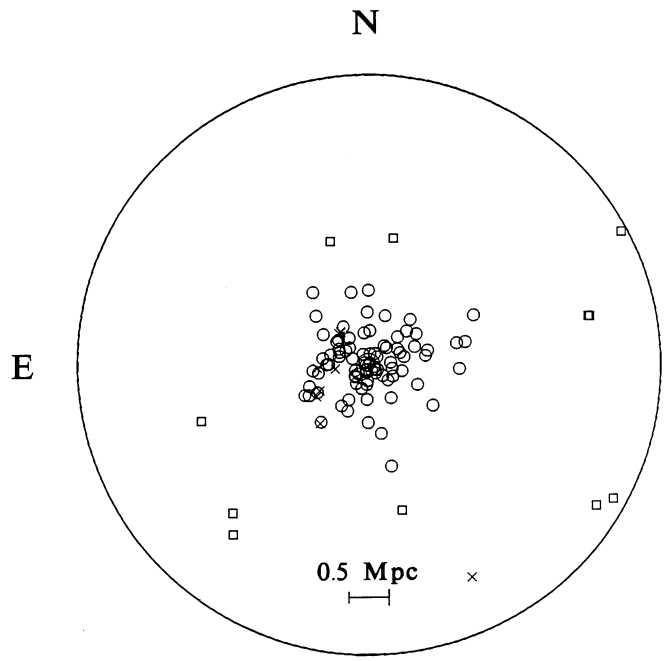

FIG. 1.—Locations of galaxies with measured radial velocities in the present sample, and projected with 3° of the dumbbell galaxy near the center of A400. The open circles indicate galaxies with heliocentric velocities within ± 4000 km s^{-1} of the dumbbell galaxy, and within a distance of 1.5 h^{-1} Mpc from the dumbell galaxy. The open squares indicate galaxies with heliocentric velocities within ± 4000 km s^{-1} of the dumbbell galaxy, but farther than 1.5 h^{-1} Mpc from the dumbbell galaxy. The crosses indicate background galaxies. The bar indicates a 0.5 h^{-1} Mpc scale at the cluster redshift.

the number of spectra obtained for the repeat galaxies in column (8). The derived velocities for these galaxies are averages of the velocities obtained from the individual spectra. The galaxy number assigned by Dressler (1980) is listed in column (9). The group assignments for the Dressler sample galaxies obtained from our kinematic cluster analysis (described below) are indicated in column (10).

There are seven galaxies in common between the Tillinghast measurements and the Medusa spectrograph measurements of Hintzen et al. (1982). The velocity differences between these galaxies are $V_T - V_H = 98$ km s^{-1}, with an rms of 81 km s^{-1}, consistent with zero to within the reported measurement errors.

3. KINEMATIC AND SPATIAL ANALYSIS

3.1. *The Complete Velocity Sample*

In Figure 1 we show positions for the galaxies in A400 with measured redshifts and projected distances within 3° of the cluster center. In Figure 2*a* we show the velocity histogram for the 88 galaxies in sample A. Figure 2*b* is the histogram for the 11 sample B galaxies. If we ignore the single extreme velocity galaxy (No. 87 in our sample), the standard tests for normality cannot reject the Gaussian hypothesis. Although the histogram of radial velocities suggests possible bimodality, the Dip test (Hartigan & Hartigan 1985) cannot reject the unimodal hypothesis. However, there are several hints that the undelying population may be more complex. Figure 3 is a stripe density plot of the velocity distribution for the 88 sample A galaxies. Each vertical line corresponds to the location of a single galaxy in velocity space. There are two significantly large gaps in the ordered velocities, indicated by the arrows (see Beers et al. 1991 and references therein for a description of gapping). One gap, of size roughly 100 km s^{-1}, occurs between galaxies 68 and 26, near the middle of the sample. According to the simulation results of Wanier & Schacht (1978), the probability of finding a normalized gap of this size ($z_* = 2.70$) is only 0.014. The other gap is between the high end of the central velocity distribution and galaxy 87, and is on the order of 1600 km s^{-1}. The probability of a normalized gap this large ($z_* = 2.39$) is 0.03. These probabilities are the "per gap" probabilities, and should not be confused with the probability of finding gaps this large *somewhere* in the distribution (with 87 independent gaps, the cumulative probabilities are not statistically significant). The existence of a large gap near the center of the distribution makes us suspicious that we are not sampling from a unimodal

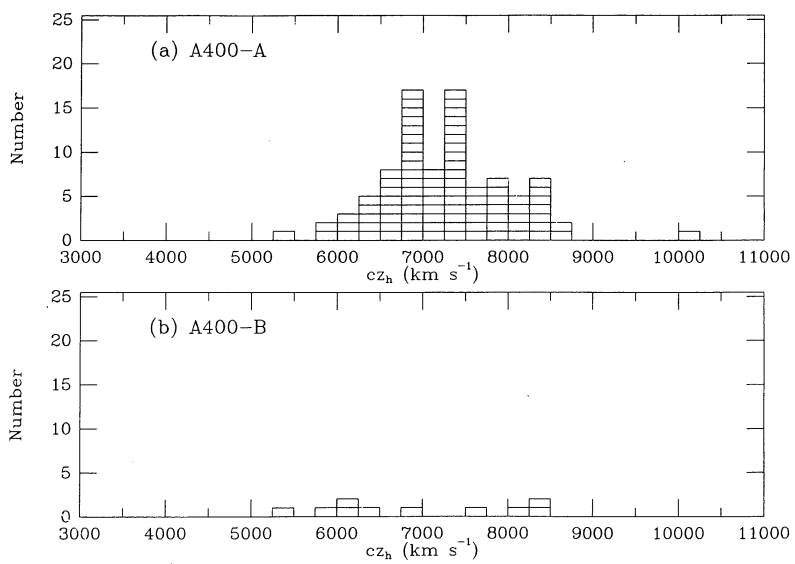

FIG. 2.—(*a*) Histogram of radial velocities for galaxies in sample A. Bins are 250 km s^{-1} in width. (*b*) Histogram of radial velocities for galaxies in sample B. Bins are 250 km s^{-1} in width.

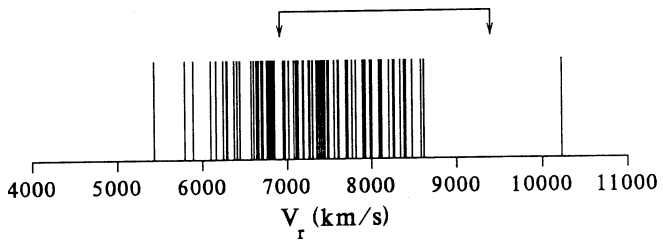

FIG. 3.—Stripe density plot of radial velocities for galaxies in sample A. The arrows indicate the location of statistically significant weighted gaps in the distribution.

distribution. An independent analysis of the velocity data in the present paper seems to confirm the existence of a complicated underlying distribution. Roeder (1991) applies a new, sensitive exploratory test for multimodality to our A400 data which suggests that the sample A galaxies are drawn from a kinematic population with at least three, and perhaps four, modes.

It has been suggested (Bothun 1981; Bothun et al. 1985) that A 400 has a dispersed supercluster component dominated by spirals with somewhat higher velocity than the cluster proper. We look to confirm this effect by splitting sample A into two subsets according to morphological type, adopting the galaxy classifications of Dressler (1980) and Nilson (1973). There are 49 galaxies in sample A classified as elliptical or S0 galaxies, and 39 classified as spiral or irregular galaxies. In Figure 4*a* we show the stripe density plot for the velocities of the E+S0 galaxies in sample A (*top*), and their spatial distribution (*bottom*). In Figure 4*b* we show the corresponding plots for the spiral galaxies. Comparison of the spatial distributions of these two morphological populations reveals a striking difference. Clearly, the elliptical galaxies are rather strongly peaked toward the central region of the cluster, where the spirals are almost absent. The spirals, in contrast, occupy the periphery of the cluster, where only a few ellipticals are found.

We now consider the velocity distributions. For the elliptical subsample, the standard normality tests cannot reject the Gaussian hypothesis. The Dip test reveals no strong bimodality. There are also no significantly large gaps in the ordered velocities. However, the tail index, TI = 1.34 (see Beers et al. 1991 and references therein), indicates that the tails of the elliptical velocity distribution are rather heavily populated. Although the standard normality tests cannot strongly reject the Gaussian hypothesis for the spiral galaxies, the possible bimodality noted in the complete sample is even more evident for the spiral subsample. The Dip test rejects the unimodality hypothesis at the 1% significance level. A large and statistically significant gap, of size roughly 400 km s^{-1} ($z_* = 3.46$, $p = 0.001$), is found between galaxy 86 and galaxy 55, near the middle of the distribution. Another large gap, of size 200 km s^{-1} ($z_* = 2.41$, $p = 0.03$), is found between galaxies 55 and 74. The third gap indicated in the figure is found between galaxies 91 and 87 and is on the order of 1600 km s^{-1} ($z_* = 2.37$, $p = 0.03$). When we consider the spiral velocity distribution as a whole, the cumulative probability of finding three or more normalized gaps of this size (or larger) is 10%, which is marginally significant. The likelihood of finding one or more gaps as large as the one between galaxy 86 and galaxy 55 anywhere in the distribution is only 5%, which is significant. The tail index, TI = 0.88, also suggests the possibility of a mixture of kinematic subsystems within the spiral galaxies.

In Figure 5 we show an alternative view of the velocity data for the sample A galaxies and the elliptical and spiral sub-

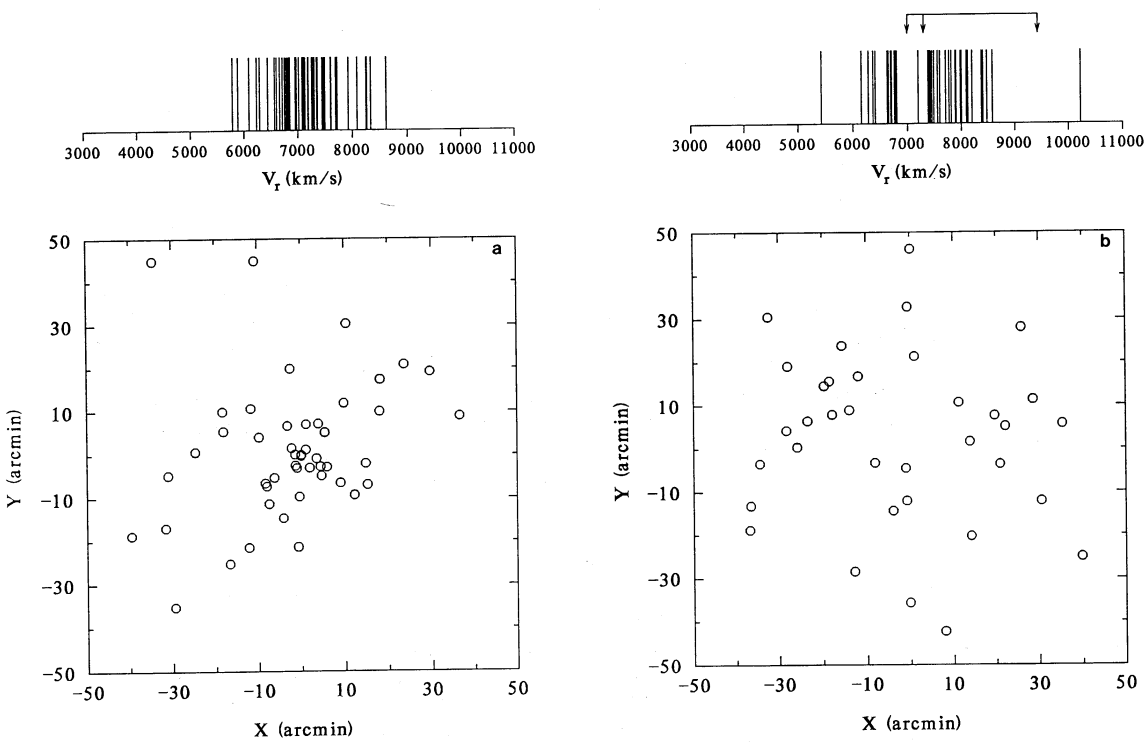

FIG. 4.—(*a*) *Top:* Stripe density plot of radial velocities for galaxies classified as elliptical or S0 in sample A. *Bottom:* Locations of galaxies classified as elliptical or S0 in sample A. (*b*) *Top:* Stripe density plot of radial velocities for galaxies classified as spiral or irregular in sample A. *Bottom:* Locations of galaxies classified as spiral or irregular in sample A.

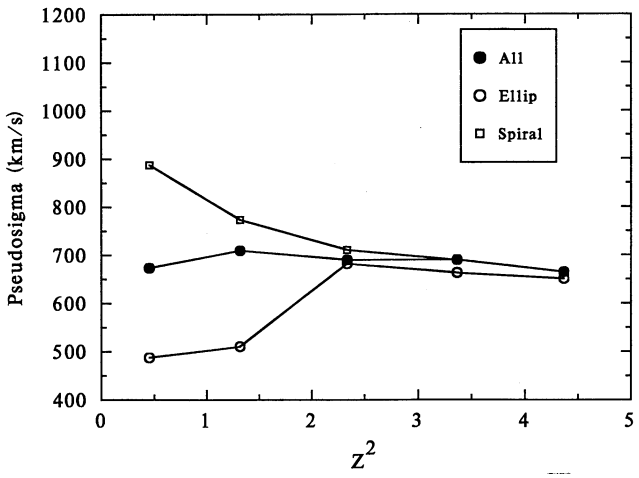

FIG. 5.—Plot of pseudosigma vs. z^2 for subsamples of radial velocities in sample A.

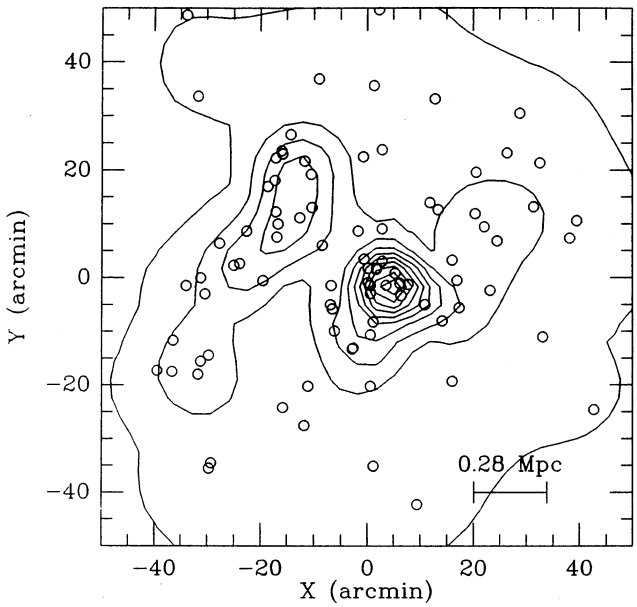

FIG. 6.—Adaptive kernel contour map of A400 for galaxies selected from the Dressler (1980) catalog within approximately 1 h^{-1} Mpc of the cluster center. The open circles indicate galaxies with measured radial velocities. The initial smoothing scale is set to 13'.9 (0.28 Mpc at the cluster redshift). Contours are linearly spaced; the lowest contour corresponds to 1 galaxy per resolution element (1.6×10^{-3} galaxies arcmin^{-2}); the highest contour is at 13.8×10^{-2} galaxies arcmin^{-2}.

samples. In this figure we show the so-called pseudosigma versus z^2 plots, discussed in detail by Hoaglin (1985). The pseudosigmas are ratios of the spread between fixed quantiles of an ordered data set relative to the standard Gaussian values. The parameter z is the standard Gaussian quantile. When a data batch is neutrally elongated relative to Gaussian, the pseudosigma versus z^2 plot follows a horizontal line because the pseudosigmas are constant. Increased elongation is shown by the rise of the pseudosigmas in the outer tails. Decreased elongation is indicated by falling pseudosigmas. As can be seen in Figure 5, the distributions classified by galaxy morphology are very different. Although the complete sample A galaxy velocity distribution appears neutrally elongated, the elliptical subsample exhibits increased elongation, while the spiral subsample exhibits decreasing elongation. A two-sample Kolmogorov-Smirnov (KS) test, which is not sensitive to this sort of difference between the two distributions, cannot reject the hypothesis that the ellipticals and spirals are drawn from the sample parent kinematic population.

In Table 2 we summarize the kinematic properties of the complete velocity sample and the elliptical and spiral subsamples. Throughout this paper, we have employed summary statistics which are robust and resistant alternatives to the traditional mean and dispersion measures (Beers, Flynn, & Gebhardt 1990). Column (1) lists the sample. Column (2) is the number of galaxies. Column (3) lists the biweight estimate of central location, C_{BI}. Column (4) lists the associated 90% bootstrap confidence interval on central location. Column (5) lists the biweight estimate of scale, S_{BI}. Column (6) lists the associated 90% bootstrap confidence interval on scale. In columns (7) and (8) we list the Dip statistic, D, and its significance level (if better than 10%). Column (9) lists the tail index, TI. As seen in the table, although the velocity distributions for the elliptical and spiral subsamples differ in statistical character, there do not exist any significant differences in their central locations or scales when compared with each other or with the sample as a whole.

3.2. *The Dressler Sample*

There is a natural bias of oversampling the high-density regions of A400 in our redshift survey, so we concentrate our subsequent analysis on the magnitude-limited sample of galaxies due to Dressler (1980). In Figure 6 we show an adaptive kernel map (Silverman 1986) of the projected number density of galaxies in the Dressler field. Superposed on this map are the locations of galaxies with measured velocities. The horizontal bar, of length 0.28 h^{-1} Mpc, indicates the size of the smoothing kernel used in the pilot density estimate. Note the suggestion of at least two apparent subclusters, features also seen in the map of Geller & Beers (1982).

TABLE 2

KINEMATICS OF THE COMPLETE VELOCITY SAMPLE

Sample	N	C_{BI} (km s^{-1})	$IC_{BC^*_{BI}}$ (km s^{-1})	S_{BI} (km s^{-1})	$IS_{BC^*_{BI}}$ (km s^{-1})	D	$p(D)$	TI
(1)	(2)	(3)	(4)	(5)	(6)	(7)	(8)	(9)
A400-A	88	7223	(−124, +131)	702	(−84, +106)	0.038	...	1.07
A400-A+B	99	7210	(−122, +129)	757	(−84, +104)	0.032	...	1.10
A400-Ellipticals	49	7068	(−128, +142)	590	(−128, +140)	0.032	...	1.34
A400-Spirals	39	7400	(−231, +210)	800	(−124, +248)	0.099	0.01	0.88

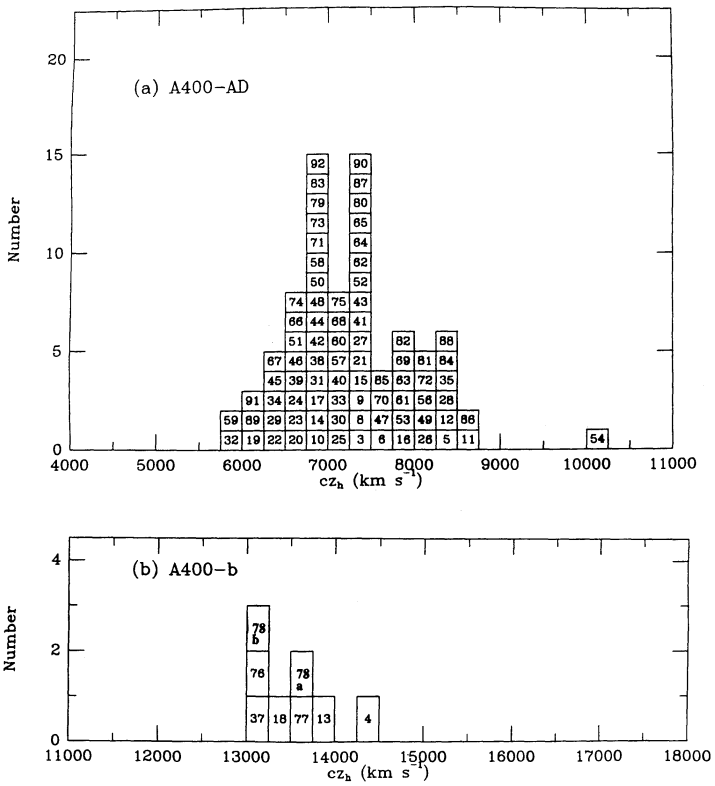

FIG. 7.—(*a*) Histogram of radial velocities for galaxies in the A400-AD sample. Numbers correspond to the Dressler galaxy identifications listed in Table 1. Bins are 250 km s^{-1} in width. (*b*) Histogram of radial velocities for galaxies in the A400-b group. Numbers correspond to the Dressler galaxy identifications listed in Table 1. Bins are 250 km s^{-1} in width.

Because of the very different spatial distributions of spirals and ellipticals in A400, the proximity of this cluster to the Perseus/Pisces supercluster, and the lack of confirming structure in the X-ray map (see § 4), we must first consider the possibility that the apparent structures in Figure 6 might be due to foreground/background contamination. We therefore choose to cluster the data initially on velocity alone, and then look to spatial information (and, to a limited extent, morphological types of proposed member galaxies) for support of our proposed splits in velocity space.

In Figure 7*a* we show the velocity histogram for the 80 Dressler galaxies included in sample A (hereafter referred to as subsample A 400-AD). The numbers within each box correspond to the original Dressler (1980) numbers, also listed in Table 1. In Figure 7*b* we show the eight Dressler galaxies which are located at around 13,400 km s^{-1}. Note that Dressler galaxy 78 is split into two nearby components, which we refer to as galaxies 78a and 78b, respectively. There is one additional Dressler galaxy, No. 36, which is located at 31,119 km s^{-1} (and is not shown in this figure).

Although the standard normality tests cannot reject the Gaussian hypothesis for the A400-AD galaxies, there are several hints that the velocity distribution may be drawn from a kinematically complex parent population. The statistically large gaps between measured velocities discussed above for the complete velocity sample remain present when the A400-AD sample is considered. In Figure 8*a* we show a histogram of the A400-AD distribution, with the best-fit single component Gaussian superposed. Deviations of the observed distribution from the Gaussian model are shown in Figure 8*b*, which is a plot of the so-called double-root residuals (DRRs) as a function of velocity (see Gebhardt & Beers 1991 for a discussion of the DRR plot). As seen in Figure 8*b*, there are three local peaks in the observed data where the disagreements with a Gaussian model are rather large (though none are significant at the 5% level). There also exists at least one sizable deficit of observed galaxies relative to the model. Below we identify the three local peaks with the central locations in velocity space of three individual groups.

3.2.1. *The Proposed Velocity Partitions*

Objective splits of univariate data into possible groups can be done in a computationally efficient manner. We make use of the clustering algorithm "partitioning around medoids" (PAM) described in detail by Kaufman & Rousseeuw (1990). Briefly, the PAM algorithm works as follows. PAM seeks k clusters of objects which have a high degree of similarity, while maximizing the degree of dissimilarity between different clusters. The algorithm initially partitions the data set into clusters around k so-called representative objects, the medoids. In a sense, PAM is similar to the well-known *k-means* clustering algorithm. However, PAM is more robust to outliers, and enjoys the additional computational advantage that it obtains

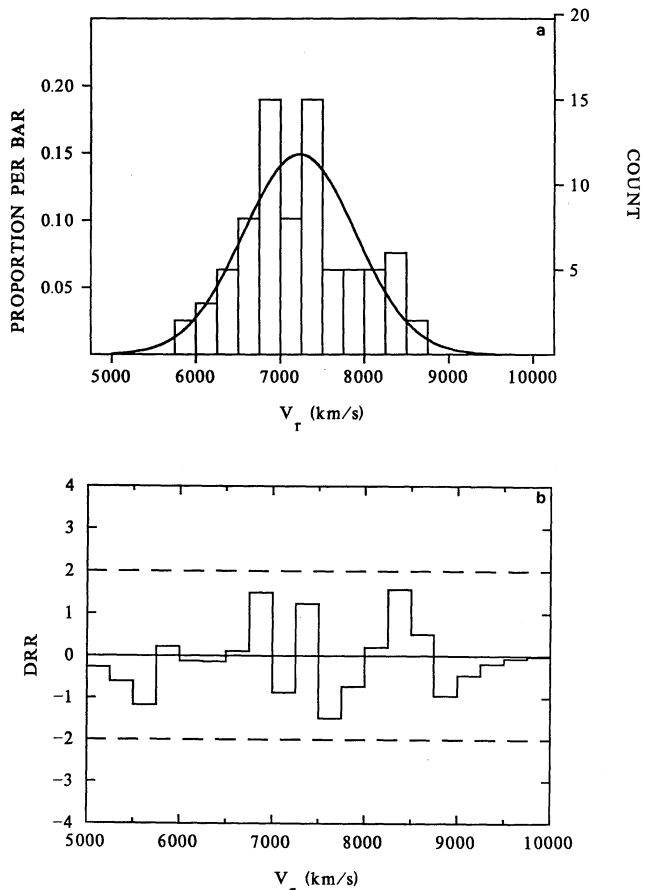

FIG. 8.—(*a*) Histogram of radial velocities for galaxies in the A400-AD sample. Bins are 250 km s^{-1} in width. The solid line is the maximum-likelihood (ML) Gaussian fit. (*b*) Double root residual (DRR) plot for the ML Gaussian fit. The dashed lines at ±2 indicate an approximate 95% significance level.

a unique partitioning of the data without the need of considering multiple starting points for the representative objects.

The quality of the resulting partitions selected by PAM is assessed by inspection of the dimensionless parameter $s(i)$, which takes on values in the range $-1 \leq s(i) \leq 1$. The parameter $s(i)$ measures the similarity of a given datum i to its closest representative object relative to its next nearest representative object. If $s(i)$ is large, we can reasonably conclude that the datum is well classified. When $s(i)$ is close to zero, it is not clear to which representative object datum i should be assigned. If $s(i)$ is close to -1, we can safely conclude that the datum i has been misclassified. Once a successful partition of the data has been achieved, we can inspect the following summary values: (1) $\bar{s}(i)$, the average of $s(i)$ within a given cluster, and (2) $\bar{s}(k)$, the average of $s(i)$ for the entire data set. This last number provides some guidance as to what value of k is most appropriate for a given data batch, i.e., the number of clusters is chosen such that $\bar{s}(k)$ is a maximum.

Table 3 summarizes the results of the PAM analysis for different input numbers of clusters $2 \leq k \leq 6$. Column (1) lists the number of clusters. Column (2) lists the number of galaxies assigned to each partition. Column (3) lists the velocity coordinate of the representative object nearest the center of each proposed cluster. The diameter (range) in velocity space covered by the proposed cluster is listed in column (4). The separation between the extrema in velocity of each cluster and its nearest (nonmember) neighbor in velocity space is listed in column (5). A seen in the table, the first split suggested by PAM differentiates the background group at $cz_h \approx 13{,}500$ km s^{-1} from the lower velocity galaxies which form the main body of the cluster. The summary statistic $\bar{s}(2)$ indicates that this is a highly significant split. When we allow PAM to find three clusters, it identifies the lone extreme galaxy as an isolated (diameter zero) entity. For $k = 4$, PAM splits the low-velocity group into two pieces, one at $cz_h \approx 7700$ km s^{-1} and the other at $cz_h \approx 6800$ km s^{-1}. Although the summary statistic $\bar{s}(4)$ drops to 0.57, this is still a rather strong clustering signal. For $k = 5$, PAM splits up the group at 7700 km s^{-1} into two entities, one at $cz_h \approx 7400$ km s^{-1}, and one at $cz_h \approx 8300$ km s^{-1}. The summary statistic $\bar{s}(5)$ is somewhat higher for this split. Finally, when $k = 6$, PAM splits off a low-velocity group at $cz_h \approx 6200$ km s^{-1}. This final split may or may not be desirable. Inspection of sample B in Figure 2 indicates that there is indeed evidence for lower velocity galaxies around $cz_h \approx 6000$ km s^{-1} in the outer regions of the cluster. However, the summary statistics in Table 3 are not greatly improved by this last split. We also find that the spatial locations of the galaxies in this final split are indistinguishable from the remaining galaxies in the group at $cz_h \approx 6700$ km s^{-1}. We prefer to terminate the PAM splits at $k = 5$. Henceforth, we refer to the subsamples identified by PAM as A400-a, A400-b, A400-c, A400-d, and A400-e, as indicated in Table 3.

3.2.2. *Kinematical, Spatial, and Morphological Properties of the Proposed Velocity Partitions*

In Figures 9*a*–9*d* we show stripe plots of the velocity distributions for the proposed splits, along with the locations of the galaxies in each split. As seen in this figure, groups A400-a and A400-d are both centrally concentrated and nearly coincident on the sky, even though their locations in velocity space differ by some 700 km s^{-1}. Group A400-b is composed exclusively of galaxies in the eastern half of the cluster, and is elongated along a north-south axis. Group A400-c only has one galaxy located near the apparent center of the western subcluster seen in Figure 6; the remaining galaxies are located in the outer regions. A substantial number of the A400-c galaxies are in the vicinity of the apparent eastern subcluster. The isolated galaxy which makes up the singleton group A400-e (not shown in Fig. 9) is also located to the east of the primary subclusters.

In Table 4 we summarize the kinematic properties of the

TABLE 3

CLUSTER ANALYSIS RESULTS: PARTITIONING AROUND MEDOIDS

k	Number	Coordinate (km s^{-1})	Diameter (km s^{-1})	Separation (km s^{-1})	$\bar{s}(i)$	$\bar{s}(k)$
(1)	(2)	(3)	(4)	(5)	(6)	(7)
2	80	7200	4435	2979	0.90	0.86
	9	13521	17913	2979	0.55	
3	80	7200	4435	2979	0.86	0.86
	8	13521	1236	2979	0.93	
	1	31118	0	16677	0.00	
4	39	7709	2966	60	0.44	0.57
	8	13521	1236	2879	0.92	
	41	6767	1409	60	0.65	
	1	31118	0	16677	0.00	
5	29	7386 (a)	737	60	0.63	0.59
	8	13521 (b)	1236	2979	0.91	
	17	8255 (c)	2331	79	0.50	
	34	6708 (d)	1228	60	0.55	
	1	31118 (e)	0	16677	0.00	
6	28	7386	712	25	0.55	0.60
	8	13521	1236	2979	0.91	
	17	8255	2331	79	0.49	
	25	6790	503	25	0.68	
	10	6243	653	132	0.55	
	1	31118	0	16677	0.00	

NOTE.—Groups a and d comprise the subsystem A400-ADL; group c is A400-ADH.

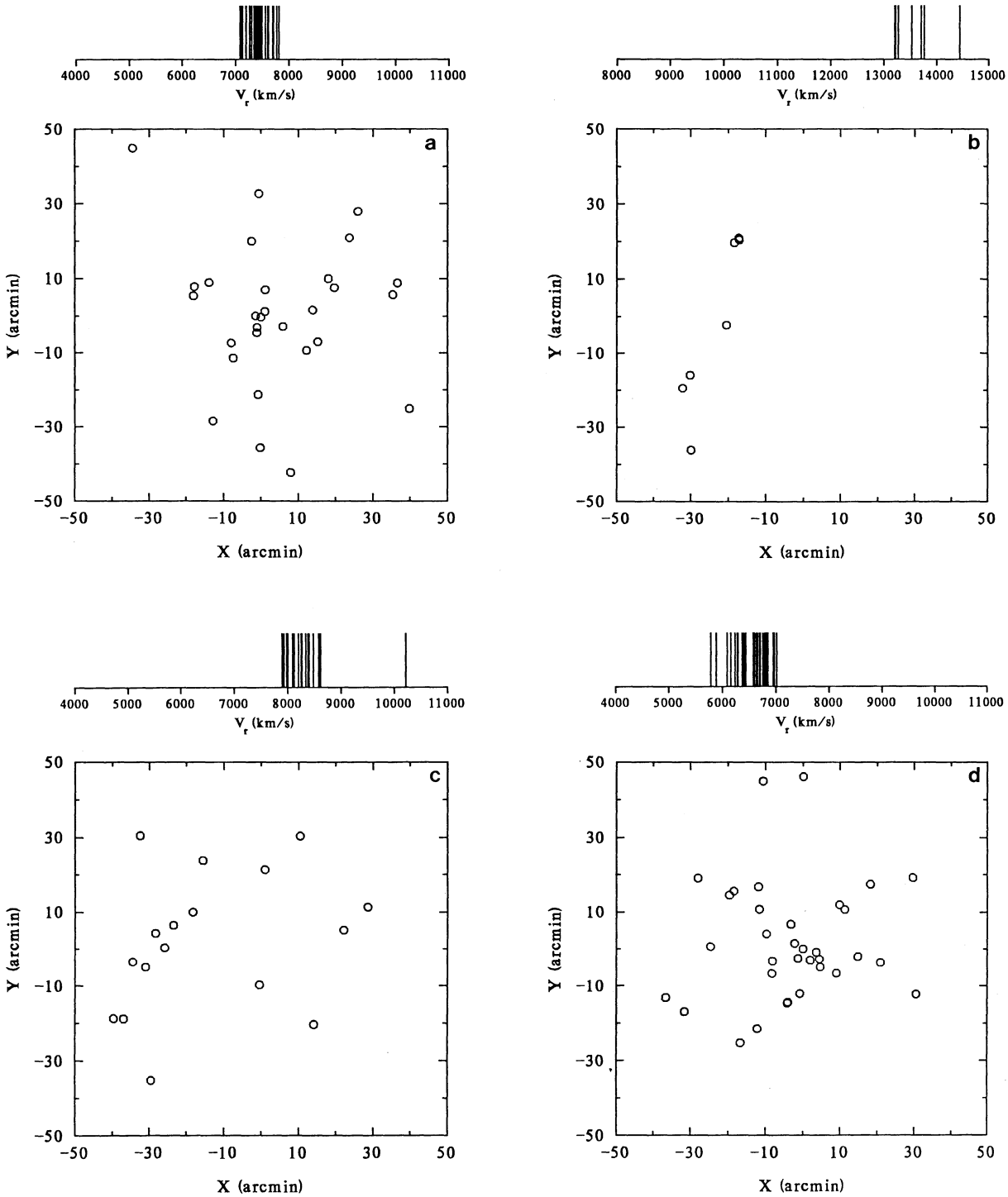

FIG. 9.—(*a*) *Top:* Stripe density plot of radial velocities for galaxies assigned to group a by the PAM analysis. *Bottom:* Locations of galaxies assigned to group a. (*b*) *Top:* Stripe density plot of radial velocities for galaxies assigned to group b by the PAM analysis. *Bottom:* Locations of galaxies assigned to group b. (*c*) *Top:* Stripe density plot of radial velocities for galaxies assigned to group c by the PAM analysis. *Bottom:* Locations of galaxies assigned to group c. (*d*) *Top:* Stripe density plot of radial velocities for galaxies assigned to group d by the PAM analysis. *Bottom*: Locations of galaxies assigned to group d.

proposed splits. Column (1) lists the sample. Column (2) lists the number of galaxies in each sample. Column (3) lists the biweight estimate of central location C_{BI}. Column (4) lists the associated 90% bootstrap confidence interval on central location. Column (5) lists the biweight estimate of scale S_{BI}. Column (6) lists the associated 90% bootstrap confidence interval on scale. In column (7) we list the fraction of galaxies in each group classified as spiral or irregular galaxies by Dressler (1980).

The first group we consider is the entire set of 80 Dressler galaxies belonging to sample A400-AD. Note that the velocity scale obtained for this sample is rather high, $S_{BI} = 711$ km s^{-1}. The spiral fraction is $f_{Sp} = 0.44$.

We now consider whether the splits suggested by the PAM

TABLE 4

KINEMATICS AND SPIRAL FRACTIONS OF POSSIBLE SUBCLUSTERS

Sample	N	C_{BI} (km s^{-1})	$IC_{BC^*_{BI}}$ (km s^{-1})	S_{BI} (km s^{-1})	$IS_{BC^*_{BI}}$ (km s^{-1})	Spiral Fraction
(1)	(2)	(3)	(4)	(5)	(6)	(7)
A400–AD	80	7206	(−128, +147)	711	(−85, +117)	0.44
A400–ADL	63	6992	(−115, +92)	486	(−54, +78)	0.38
A400–ADH	17	8224	(−113, +96)	245	(−44, +221)	0.65
A400–Group a	29	7386	(−33, +67)	212	(−35, +47)	0.41
A400–Group b	8	13409	(−197, +337)	369	(−333, +375)	0.50
A400–Group c	17	8224	(−113, +96)	245	(−44, +221)	0.65
A400–Group d	34	6709	(−158, +76)	283	(−107, +110)	0.35
A400–Group e	1	31118	...	...	...	...

analysis are reasonable by examination of an intermediate split of the A400-AD sample into two groups. We identify the sample A400-ADL, comprised of the proposed subclusters A400-a and A400-d. The sample A400-ADH is identified with the proposed subcluster A400-c. In Figures 10*a* and 10*b* we show the velocity and spatial distributions of galaxies in these proposed splits. The spatial distributions of the elliptical and spiral galaxies in A400-ADL are rather similar. The velocity scale of A400-ADL, $S_{BI} = 486$ km s^{-1}, is substantially smaller than that of the entire A400-AD sample. The velocity scale of A400-ADH, $S_{BI} = 245$ km s^{-1}, is also quite small. The central locations in velocity space of A400-ADL and A400-ADH differ by some 1200 km s^{-1}.

In Figure 11 we show the stripe density plot and histogram of the velocity distribution for galaxies in A400-ADL. Although the standard normality tests cannot reject the Gaussian hypothesis, there exist two significantly large gaps in the distribution, indicated by the arrows in the stripe density plot. The gap between galaxies 41 and 70 is roughly 130 km s^{-1} ($z_* = 2.42$, $p = 0.03$), while that between galaxies 68 and 26 is on the order of 100 km s^{-1} ($z_* = 2.86$, $p = 0.006$). The probability of finding two or more normalized gaps this large somewhere in the distribution is 0.31, which is not significant.

Figure 12 shows similar stripe plots and histograms of the velocity distributions for the elliptical and spiral galaxies of A400-ADL. Several interesting differences are apparent. Although the ellipticals have no statistically significant normalized gaps, their velocity distribution is rather skew. The sample skewness coefficient $\beta_1^{1/2}$ is equal to -0.63, which allows rejection of the Gaussian hypothesis at the 0.04 level of significance. There is no clear evidence in the histogram for multiple modes, an impression confirmed by a small Dip statistic, $D = 0.04$. The velocity distribution of spirals in A400-ADL exhibits three large gaps, indicated by arrows. The first gap, between galaxies 61 and 53, is on the order of 180 km s^{-1} ($z_* = 2.46$, $p = 0.03$). The second gap, between galaxies 86 and 55, is roughly 400 km s^{-1} ($z_* = 4.36$, $p = 0.0005$). The third gap, between galaxies 55 and 74, is on the order of 220 km s^{-1} ($z_* = 2.97$, $p = 0.006$). The likelihood of finding three or more normalized gaps this large is rather small, $p = 0.01$, if we are sampling from a single Gaussian population. The Dip statistic, $D = 0.122$, is significant at the 0.01 level, which confirms the impression of bimodality in the velocity histogram.

Although the velocity distributions of the elliptical and spiral galaxies in A400-ADL appear quite different, the offsets in central location [$C_{BI}(\mathrm{El}) = 7050^{+278}_{-221}$ km s^{-1}; $C_{BI}(\mathrm{Sp}) = 6973^{+104}_{-153}$ km s^{-1}] and scale [$S_{BI}(\mathrm{El}) = 522^{+99}_{-68}$ km s^{-1}; $S_{BI}(\mathrm{Sp}) = 442^{+122}_{-85}$ km s^{-1}] are not significant. A two-sample KS test cannot reject the hypothesis that the elliptical and spiral galaxies are drawn from the same parent population.

Taken as a whole, our detailed examination of the character of the velocity distribution within A400-ADL suggests that the split into the two groups A400-a and A400-d is warranted. Further support is obtained below by consideration of the derived masses and mass-to-light ratios for A400-ADL versus the values obtained for the A400-a and A400-d subclusters. When we consider the groups identified by the PAM analysis with $k = 5$, the velocity scales of the individual groups fall to $S_{BI} \approx 200$–350 km s^{-1}. The spiral fractions of A400-a and A400-d are similarly small, on the order of 0.35–0.40. The spiral fraction of group A400-c (identical to the sample A400-ADH) is substantially higher. The background group A400-b has a spiral fraction $f_{Sp} = 0.50$.

3.2.3. *Mixture Model Analysis*

Our proposed velocity splits represent "hard" clusters within the data; as a result it is possible that we have truncated the tails of the component subpopulations, which might lead us to underestimate their true velocity scales. We obtain limits on the magnitude of possible scale underestimates for A400-a and A400-d by fitting a mixture model distribution to the velocity data, assuming that the individual component distributions represent random draws from Gaussian parent populations. We employ the methodology described by McLachlan & Basford (1988), in which one obtains a maximum-likelihood estimate of the mixing distribution given an initial partition of the data. The program KMM, kindly provided to us by G. J. McLachlan, allows one to restrict the solution to either the case that the proposed k groups share a common covariance matrix (i.e., identical scales) or else the case in which they have independent covariance matrices (nonidentical scales). Maximum-likelihood (ML) solutions with a common covariance matrix have the advantage that the ML peak is well defined and unique. In the case of independent covariance matrices, the ML solution is generally one of many possible similar-sized peaks in the solution space, and is thus subject to small perturbations in the initial specification of the model.

The hard clusters obtained by PAM (see Table 3) are used as the initial partition of the data required by KMM. We obtain mixture model results for the cases of two, three, and four groups within the main body of the A400-AD data (5000 km

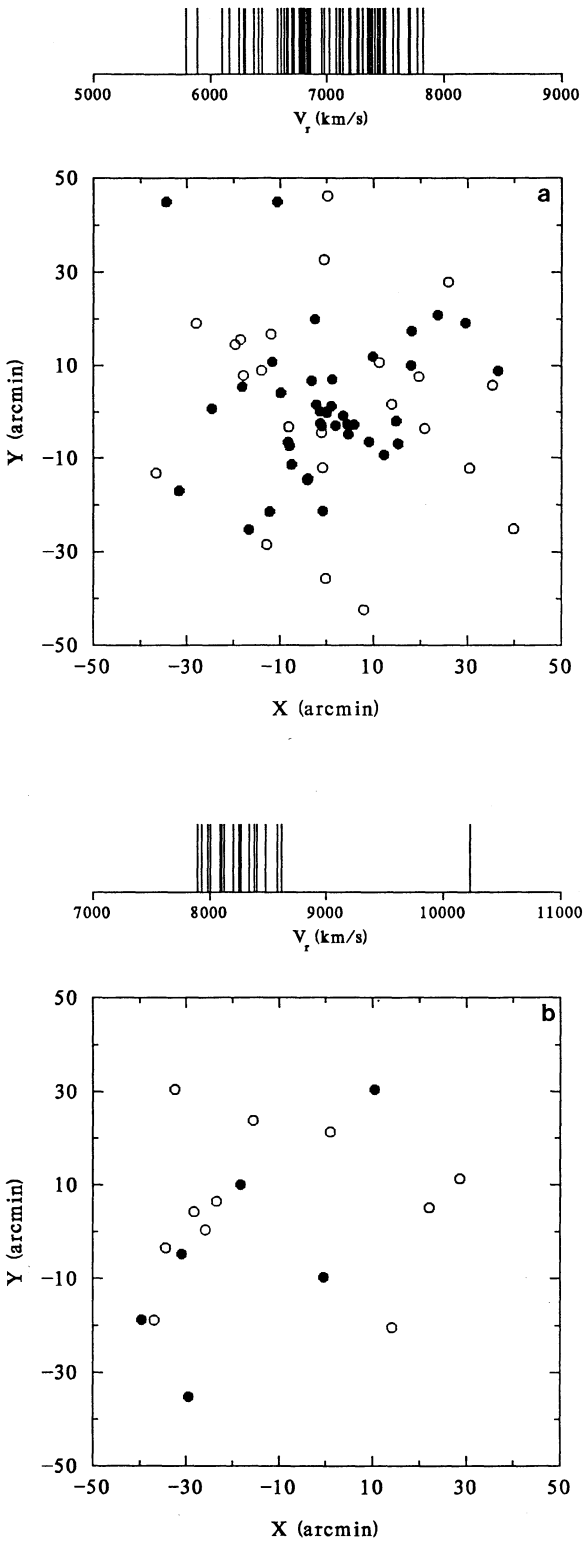

FIG. 10.—(*a*) *Top:* stripe density plot of radial velocities for galaxies in the system A400-ADL (A400-a plus A400-d). *Bottom:* Locations of galaxies in A400-ADL. Filled circles indicate galaxies classified as elliptical or S0. Open circles indicate galaxies classified as spiral or irregular. (*b*) *Top:* Stripe density plot of radial velocities for galaxies in the system A400-ADH (A400-c). *Bottom:* Locations of galaxies in A400-ADH. Filled circles indicate galaxies classified as elliptical or S0. Open circles indicate galaxies classified as spiral or irregular.

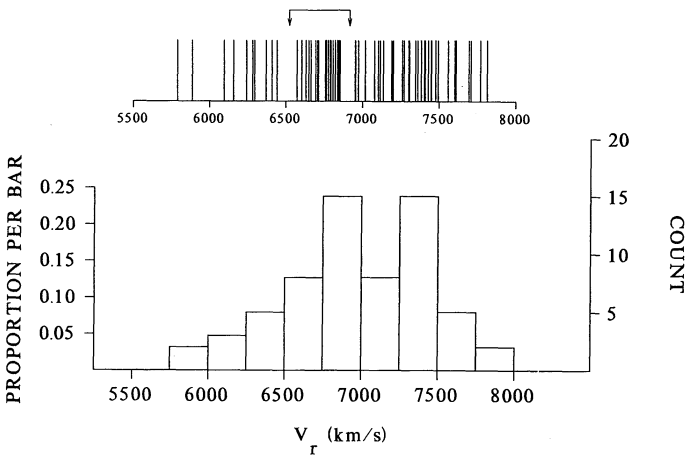

FIG. 11.—*Top:* Stripe density plot of radial velocities for galaxies in the system A400-ADL (A400-a plus A400-d). Arrows indicate the location of statistically significant normalized gaps in the distribution. *Bottom:* Histogram of radial velocities in A400-ADL. Bins are 250 km s^{-1} in width.

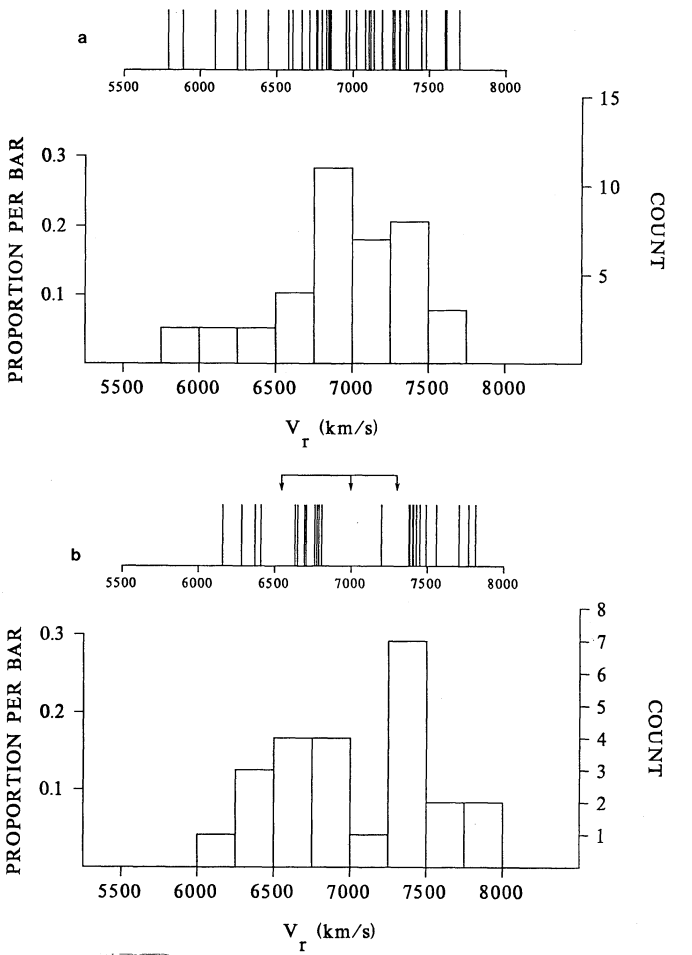

FIG. 12.—(*a*) *Top:* Stripe density plot of radial velocities for elliptical and S0 galaxies in the system A400-ADL (A400-a plus A400-d). *Bottom:* Histogram of radial velocities for elliptical and S0 galaxies in A400-ADL. Bins are 250 km s^{-1} in width. Note the apparently skew nature of the velocity histogram. (*b*) *Top:* Stripe density plot of radial velocities for spiral and irregular galaxies in the system A400-ADL. Arrows indicate the location of statistically significant normalized gaps in the distribution. *Bottom:* Histogram of radial velocities for elliptical and S0 galaxies in A 400-ADL. Bins are 250 km s^{-1} in width. Note the apparent bimodal nature of the velocity histogram.

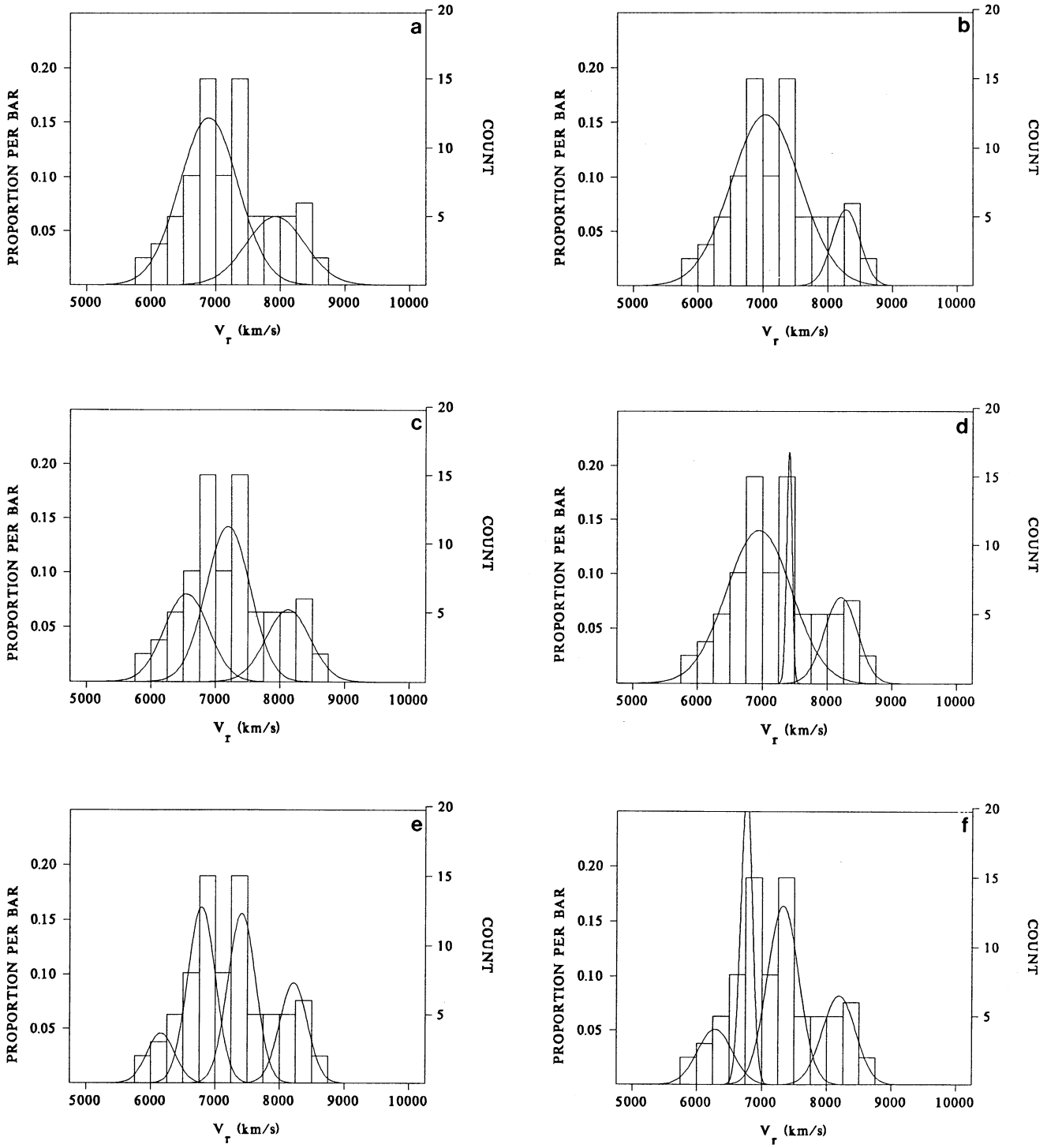

FIG. 13.—Results of model fits of the A400-AD velocity data to mixtures of Gaussian populations. (*a*) Two groups with common scales. (*b*) Two groups with independent scales. (*c*) Three groups with common scales. (*d*) Three groups with independent scales. (*e*) Four groups with common scales. (*f*) Four groups with independent scales. The fit shown in (*e*) is the only one which is a statistically significant improvement over the hypothesis of a single group.

$s^{-1} \leq cz_h \leq 10{,}000$ km s^{-1}). These results are shown in Figures 13*a*–13*f*. Note that when independent scales are allowed for the components of the mixtures, in the case of three groups (Fig. 13*d*) and four groups (Fig. 13*f*), at least one of the resulting components has an extremely low scale, less than 100 km s^{-1}. For the case of four groups with common scales (Fig. 13*e*), the value of the likelihood ratio test statistic, which can be taken as an indication of the degree to which the model fit is improved over the hypothesis of a single component, is 10.68 with 6 degrees of freedom. According to the approximations of Wolfe (1971), this increase is significant at the 10% level. None of the other cases achieved similarly high levels of significance.

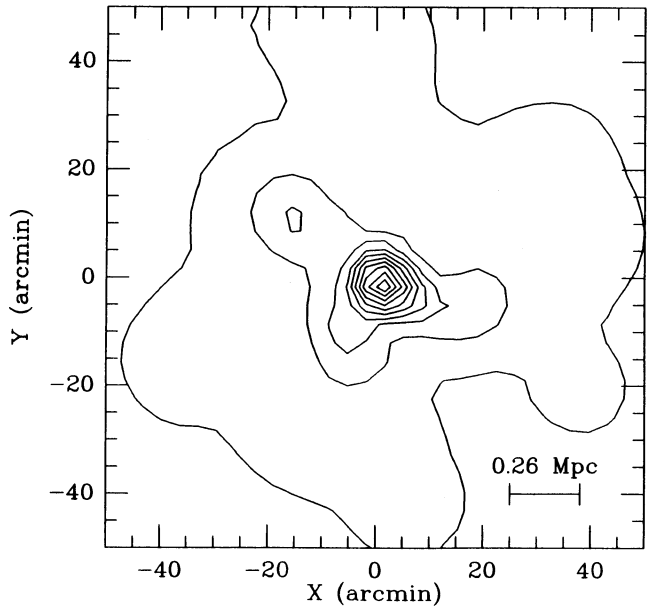

FIG. 14.—Adaptive kernel contour map of A400 for galaxies assigned to sample A400-ADL (groups a and d) by the PAM analysis. The initial smoothing scale is set to 13.1 (0.26 h^{-1} Mpc at the cluster redshift). Contours are linearly spaced; the lowest contour corresponds to 1 galaxy per resolution element (1.9×10^{-3} galaxies arcmin^{-2}); the highest contour is at 15.8×10^{-2} galaxies arcmin^{-2}.

The scales obtained for the case of two, three, and four groups (common covariance matrices) were 453, 342, and 216 km s^{-1}, respectively. We conclude that, if our division of the main body of the A400-AD sample into three primary velocity groups is correct, our estimates of scale for the individual components are not gross underestimates.

3.2.4. *A New Map of A400 Based on Kinematically Selected Cluster Members*

Based on the above analysis, we believe that A400 is composed of at least two primary subclusters, which we call A400-a and A400-d; a dispersed (spiral-rich) component, which we call A400-c; and a background group, which we call A400-b. In Figure 14 we show an adaptive kernel map of A400 based exclusively on the galaxies which are members of the subclusters A400-a and A400-d. The apparent subcluster to the east seen in Figure 6 has now all but disappeared from this map.

4. X-RAY ANALYSIS OF A400

4.1. *The X-Ray Map of A400*

Figure 15 is a plot of the X-ray surface brightness distribution of the hot intracluster gas associated with A400, obtained with the IPC detector on board the *Einstein* satellite. The contour map is superposed on an enlargement of the Palomar Sky Survey. As seen in this figure, there is no apparent X-ray emission associated with the loose distribution of (predominantly) spiral galaxies to the north and east. This map does agree rather well, however, with the central region of the

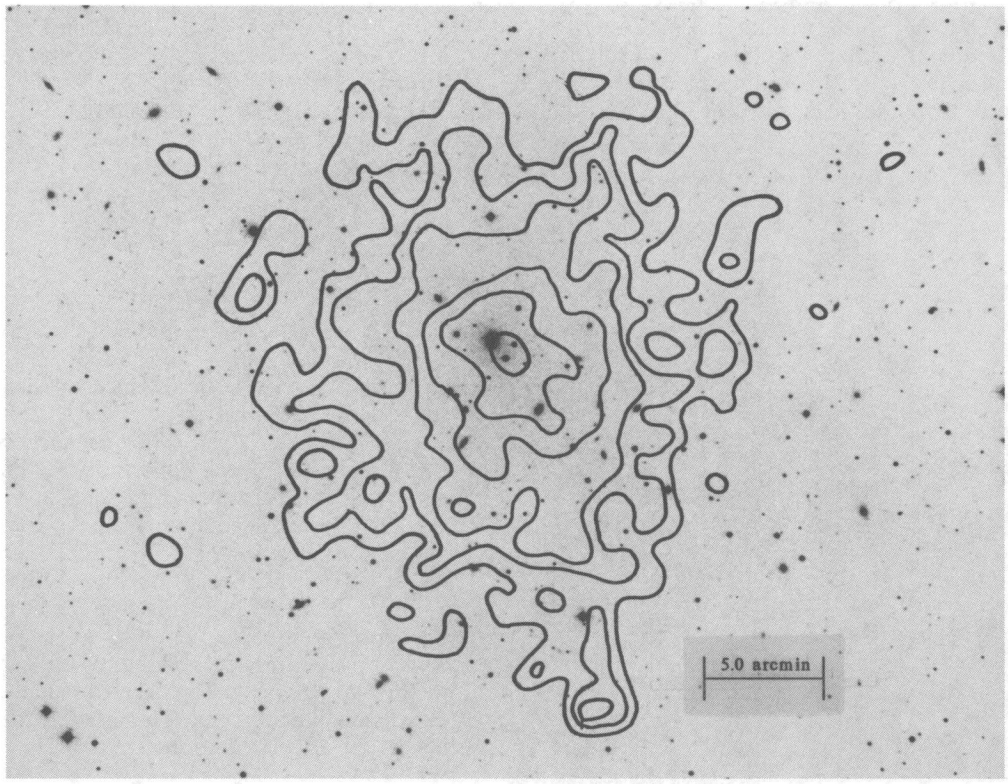

FIG. 15.—IPC X-ray contour map of A400 reproduced from Jones & Forman (1992). The contours are generated from the 0.5–4.5 keV images smoothed with a Gaussian kernel ($\sigma = 32''$). The contour map is superposed on optical images taken from the Palomar Sky Survey; centering is accurate to $\sim 1'$. Note the marked asymmetry of the emission in the central region of the cluster and the lack of emission to the north and east.

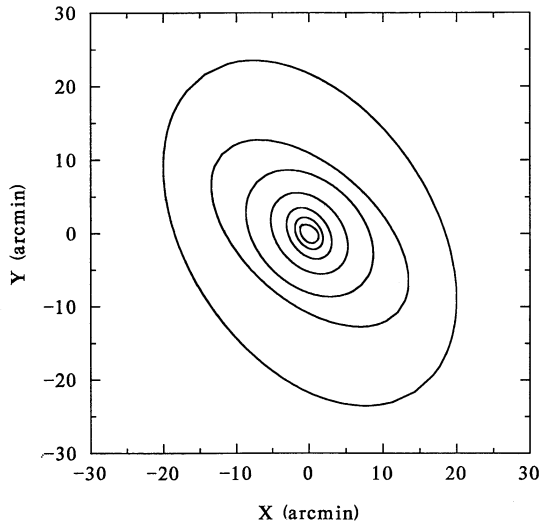

FIG. 16.—Elliptical contour fits obtained for *Einstein* IPC map of A400. Every fifth ellipse is shown, along with the distribution of centers of the individual ellipses (*crosses*). Note that the ellipticity remains relatively constant from the central to the outer regions of the fit, while the orientation angle exhibits a slight rotation.

adaptive kernel map of A400 based on members of subclusters A400-a and A400-d alone, shown in Figure 14. It is also clear from Figure 15 that the X-ray emission is somewhat elliptical, with a major axis oriented in a northeast-southwest direction. We have fitted the X-ray image of A400 using the PROS task ELLIPSE, after applying a modest smoothing to the data. Figure 16 is a plot of the elliptical contours obtained with this procedure. Figure 17 is a plot of the orientation of the elliptical contours (as measured counterclockwise from the north) as a function of the semimajor axis. No significant offset of the centers of the elliptical isophotes from the central to the outer region was obtained.

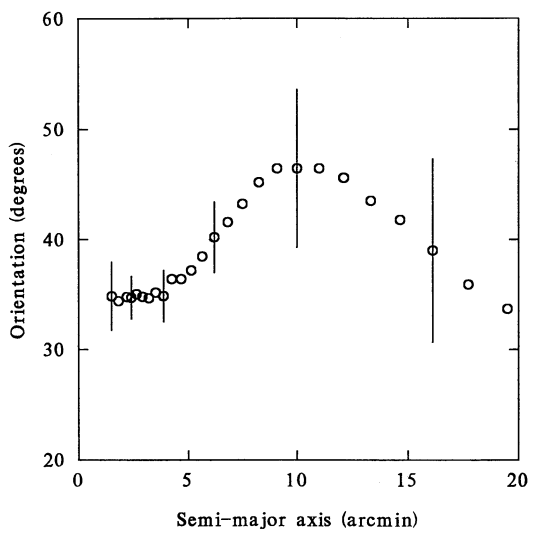

FIG. 17.—Orientation angle (as measured counterclockwise from the north) of the elliptical fit of the A400 X-ray surface brightness distribution as a function of the semimajor axis of the individual ellipses. Error bars are shown for every fifth point.

4.2. *Estimates of Physical Parameters for the A400 Intracluster Medium*

We obtain simple parameterizations of the spatial distribution of the X-ray–emitting gas in A400 by fitting single- and multiple-peaked gas density distributions to the observed surface brightness obtained from the background-subtracted, vignetting-corrected IPC image of A400 (effective exposure time 11,403 s). Each gas density distribution is characterized by

$$n(r) = n(0)[1 + (r/a_x)^2]^{-3\beta/2}, \quad (1)$$

where $n(0)$ is the central gas density, a_x is a characteristic radius, and β is a free parameter. If the gas temperature is approximately isothermal or the gas temperature exceeds about 2 keV (see Fabricant, Lecar, & Gorenstein 1980), the surface brightness distribution corresponding to equation (1) is

$$S(r) = S(0)[1 + (r/a_x)^2]^{-3\beta+1/2} \quad (2)$$

This form for the surface brightness distribution has been widely used to describe the X-ray emission in clusters of galaxies (e.g., Jones & Forman 1984) and has been found to be an adequate description up to 8–10 core radii in some clusters (see Henricksen & Mushotzky 1985; Briel et al. 1991; Edge & Stewart 1991b). Edge & Stewart (1991b) refer to the β parameter obtained from the above procedure as $\beta_{\rm imag}$.

If both the gas and galaxies are in equilibrium in the same gravitational potential (which may *not* be applicable for A400), and the distribution of the galaxies can be described by

$$n_{\rm gals} = n_{\rm gals}(0)[1 + (r/a_{\rm gals})^2]^{-3/2}, \quad (3)$$

then $a_{\rm gals} = a_x$, and we may obtain the parameter $\beta_{\rm spec} = \mu m_{\rm H} \sigma_{\rm los}^2 / kT_{\rm gas}$, where μ is mean molecular weight of the gas, $m_{\rm H}$ is the mass of the hydrogen atom, $\sigma_{\rm los}$ is the line-of-sight velocity dipersion of the galaxies, $T_{\rm gas}$ is the gas temperature, and k is Boltzmann's constant (Cavalier & Fusco-Femiano 1976). The central gas density is derived from the X-ray luminosity using the derived gas density parameters and assuming the gas is isothermal. In all our calculations, we have used a gas temperature for A400 of $kT = 2.5^{+0.8}_{-0.6}$ keV determined from the *Einstein* monitor proportional counter (MPC) (David 1992), which is in agreement with the *EXOSAT* measurement of 2.2 ± 1.4 keV (Edge & Stewart 1991a).

As is clear from our discussion above, we suspect that A400 harbors physical substructure which, though not clearly evident in the X-ray image, may affect our estimates of the gas parameters. We have thus obtained three different fits to the X-ray surface brightness distribution. The three models used are model 1, a single spherically symmetric component; model 2, a superposition of two spherically symmetric components having equal values of β; and model 3, a superposition of two spherically symmetric components having equal values of both β and the normalization.

The results of maximum-likelihood fits to these models (from Jones et al. 1992) are given in Table 5. Column (1) lists the model being fitted. Column (2) lists the ratio of the normalizations of the components. Columns (3) and (4) list the values of a and β, respectively. The derived values of the gas density $n(0)$ are listed in column (5). The fitted locations of the centers of the gas density distributions are given in columns (6) and (7) (epoch 1950).

Figures 18*a* and 18*b* are plots of the derived locations for the individual subclusters for models 2 and 3, respectively. The circles are drawn with sizes equal to the core radii obtained

TABLE 5

PHYSICAL PARAMETERS DERIVED FROM X-RAY OBSERVATIONS OF A400

Model (1)	Relative Normalization (2)	a (h^{-1} kpc) (3)	β (4)	$n(0)$ ($10^{-3}\ h^{1/2}\ cm^{-3}$) (5)	RA (1950) (6)	DEC (7)
1	1.0	81	0.57	1.49	02 54 58.6	+05 48 25.0
2	4.7	87	0.64	1.47	02 54 58.9	+05 49 19.7
	1.0	103	0.64	0.55	02 54 56.5	+05 42 01.1
3	1.0	75	0.61	1.30	02 54 59.4	+05 50 35.1
	1.0	88	0.61	1.04	02 54 57.8	+05 46 20.8

[a] Model 1: Single spherically symmetric cluster; a, β, and position are free parameters. Model 2: Two spherically symmetric condensations; β-values are held equal (but allowed to vary); relative normalizations, a, and positions are free parameters. Model 3: Two spherically symmetric condensations; β-values and relative normalizations are held equal (but allowed to vary); a and positions are free parameters.

from the fitting procedure. Clearly, the models we have proposed are not unique, and many possible separations, orientations, and normalizations of two (or more) X-ray–emitting components are allowed by the data. Future observations of this cluster with *ROSAT* should provide for more definitive tests of structure in the X-ray surface brightness distribution. However, the *Einstein* X-ray map certainly does not preclude the possibility that real substructure exists in A400, and, as discussed below, it provides some support for the model of the bending of the jets in 3C 75 by dynamic pressure associated with the motion of the D galaxies relative to the intracluster medium.

We consider the values of β_{spec} obtained for different subsamples of the A400-AD galaxies. If we take $\sigma_{los} = S_{BI}(\text{A400-AD}) = 711$ km s^{-1}, we derive $\beta_{spec} = 1.26^{+0.70}_{-0.50}$, similar to the high value obtained by Edge & Stewart (1991b), $\beta_{spec} = 1.06^{+0.51}_{-0.50}$. If $\sigma_{los} = S_{BI}(\text{A400-ADL}) = 486$ km s^{-1}, we derive $\beta_{spec} = 0.59^{+0.32}_{-0.19}$, a value consistent with the value of β_{imag} obtained from our analysis of the X-ray surface brightness distribution. Unfortunately, we cannot calculate β_{spec} for the proposed subclusters A400-a and A400-d because we lack a spatially resolved temperature map.

The hydrostatic, isothermal model allows a direct estimate of the binding mass within a radius r (e.g., Evrard 1990):

$$M_b(r) = 5.5 \times 10^{13} \beta_{imag} \left(\frac{T}{\text{keV}}\right)\left(\frac{r}{\text{Mpc}}\right)\frac{(r/a_x)^2}{[1+(r/a_x)]^2}\ h^{-1}\ M_\odot\ . \quad (4)$$

Adopting the single-component fit results from above ($\beta_{imag} = 0.57$, $a_x = 0.081\ h^{-1}$ Mpc) and $T = 2.5$ keV, we obtain $M_b(r = 1\ h^{-1}\ \text{Mpc}) = 7.2 \times 10^{13}\ h^{-1}\ M_\odot$.

We may also use the hydrostatic, isothermal model to obtain an estimate of the total mass of radiating gas within the cluster, as described in David et al. (1990). Adopting the single-component fit results as above, we obtain $M_{gas} = 8.5 \times 10^{12}\ h^{2.5}\ M_\odot$ within a distance of $1\ h^{-1}$ Mpc of the cluster center. This mass is on the order of 15% of the total bound mass derived above, and on the order of 10% of the dynamical mass estimates derived below, typical of results found for other rich clusters.

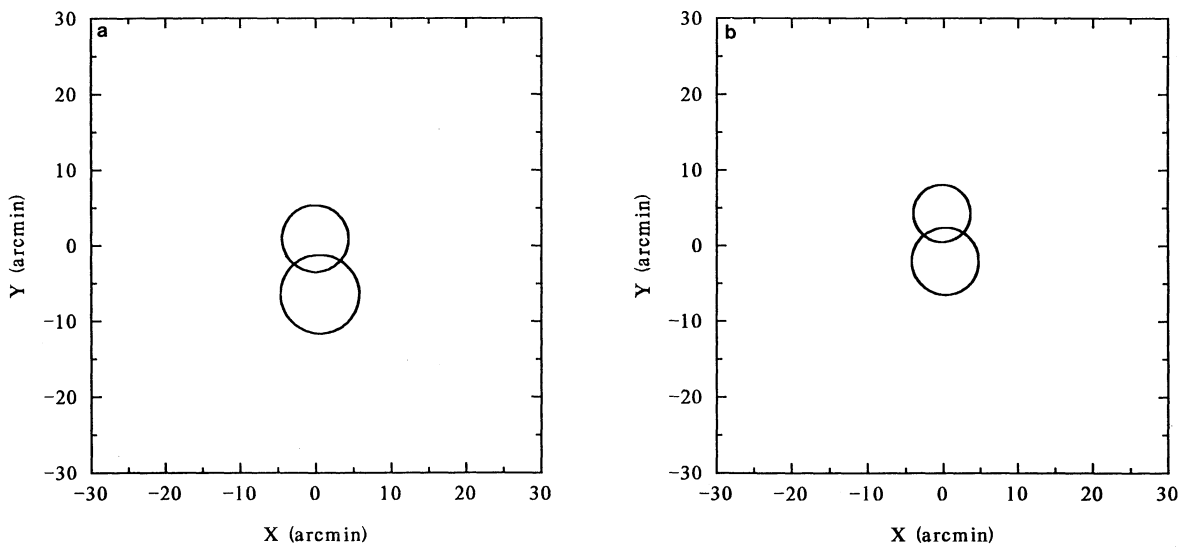

FIG. 18.—(*a*) Location of proposed centers for a two-component model of the surface brightness distribution in A400, obtained for case 2 as described in the text. The radius of each circle corresponds to the derived value of the X-ray core radius for the individual components. (*b*) As before, but for case 3 as described in the text.

TABLE 6

MASS AND MASS-TO-LIGHT ESTIMATES OF POSSIBLE SUBCLUSTERS

Sample (1)	N (2)	M_{pm} ($10^{13}\ h^{-1}\ M_\odot$) (3)	M_v ($10^{13}\ h^{-1}\ M_\odot$) (4)	M_v' ($10^{13}\ h^{-1}\ M_\odot$) (5)	$M_v'/L_{B(0)}$ ($h\ M_\odot/L_\odot$) (6)
A400-AD	80	67 ± 10	49 ± 7	44 ± 7	1210 ± 200
A400-ADL	63	24 ± 3	17 ± 2	18 ± 3	615 ± 90
A400-ADH	17	32 ± 18	33 ± 18	6.9 ± 3.8	1030 ± 550
A400-a	29	3.7 ± 0.7	3.6 ± 0.7	3.9 ± 0.8	315 ± 60
A400-d	34	8.6 ± 3.4	6.9 ± 2.7	5.8 ± 2.3	354 ± 140

5. DYNAMICAL ANALYSIS

5.1. *Mass and Mass-to-Light Estimates*

We obtain dynamical estimates of the cluster and proposed subcluster masses following the procedure outlined in Beers et al. (1991). Our results are summarized in Table 6. In column (1) we list the sample under consideration. Column (2) lists the number of galaxies in each sample. Column (3) lists the projected mass, M_{pm}, obtained under the assumption of isotropic orbits and a distributed (rather than central) mass (Heisler, Tremaine, & Bahcall 1985). In column (4) we list the standard virial mass estimate, M_v. Column (5) lists the modified virial mass estimate, M_v', obtained by forcing the cluster dispersion to equal the biweight estimate of scale, S_{BI}. Along with each mass estimate in columns (3)–(5), we list the jackknife estimate of error in its determination. With the exception of A400-ADH, where the virial and projected mass estimators are strongly influenced by a single high-velocity galaxy, the mass estimators agree well with one another.

It is of interest to note that the only dynamical mass estimates in Table 6 which are on the same order of magnitude as the X-ray binding mass estimates derived above are those obtained under the assumption that A400 is comprised of the subclusters A400-a and A400-d. When A400 is divided into the high- and low-velocity groups A400-ADH and A400-ADL, or is considered as a single dynamical entity, the derived dynamical masses are between 2 and 6 times higher than the binding mass inferred from the X-ray analysis.

Estimates of the mass-to-light ratios for the cluster and proposed subclusters are obtained as follows. The approximate V-magnitudes listed by Dressler (1980) are transformed to the Zwicky $B(0)$ scale assuming $B(0) - V = 0.9$. The corresponding luminosities (in solar units) are obtained by summing the luminosity of each galaxy in the sample, assuming that they are located at the redshift distance of their parent cluster or subcluster. We obtain the total luminosity of each sample by correcting for the luminosity contained at the faint end of the Schechter function, assuming that the knee of the luminosity function is at $M_B(0) = -19.2$ (Huchra 1991) and that the Dressler sample is complete to $V = 16.0$. In reality, the Dressler sample is probably incomplete at this magnitude, hence the total luminosities should be considered underestimates, which leads in turn to an overestimate of the mass-to light ratios.

We list the derived mass-to-light ratios, in solar units, in column (6) of Table 6. The jackknife errors listed in column (6) are certainly too low, since they do not include errors in the Dressler magnitude estimates or errors introduced by the incompleteness of the magnitude distribution in the Dressler sample. The derived mass-to-light ratio of the entire sample A400-AD is extremely large, $M/L \approx 1200\ h\ M_\odot/L_\odot$. Even when the sample is subdivided into A400-ADL and A400-ADH, the derived mass-to-light ratios remain high, $M/L \approx$ 600–1000 $h\ M_\odot/L_\odot$. Only when we consider the groups A400-a and A400-d individually do the mass-to-light ratios approach values considered normal for rich clusters of galaxies, $M/L \approx 300$–$350\ h\ M_\odot/L_\odot$ (Faber & Gallagher 1979; Edger & Stewart 1991b).

5.2. *Two-Body Analysis*

To obtain some insight about the current dynamical state of the A400 cluster, we carry out a series of two-body models, following the procedures outlined by BGH.

The BGH analysis assumes radial orbits for the subclusters, with no shear or net rotation of the system. Furthermore, the systems are assumed to start their evolution at time $t = 0$ with zero separation, and are moving apart or coming together for the first time in their history. The relevant geometry is shown in Figure 7 of BGH. The coupled equations which describe the time evolution of this simple model are closed by setting the present time to $t_0 = 3.1 \times 10^{17}\ h^{-1}$ s, the age of the universe as specified by $q_0 = 0$, $H_0 = 100\ h$ cosmology. The equations are solved in an iterative fashion to determine the projection angle with respect to the plane of the sky, α, as a function of the radial velocity difference between the clusters or subclusters. The system parameters V (the true spatial relative velocity difference) and R (the true spatial separation) are related to the observables V_r (the radial velocity difference) and R_p (the projected separation) by an apparent geometry: $V_r = V \sin \alpha$; $R_p = R \cos \alpha$. Simple energy considerations specify the limits of bound solutions. The Newtonian criterion for gravitational binding can be stated in terms of the observables as

$$V_r^2 R_p \leq 2GM_{\rm sys} \sin^2 \alpha \cos \alpha\ , \qquad (5)$$

independent of H_0. In the two-body model figures described below (Figs. 19 and 20), the stippled region of the (α, V_r)-plane is the region where unbound solutions must lie; the rest of the plane is the region of bound solutions.

In Table 7 we summarize the results of our two-body analyses. Column (1) lists the sample under consideration. Column (2) lists the total system mass, obtained by summing the modified virial masses of the individual subclusters. Column (3) lists the relativistically correct velocity difference between the primary subclusters of each system, $|V_r|$, and its associated 68% error. Column (4) lists the projected separation R_p. For the present application, we have obtained the projected separation from the difference in the median centroids of the galaxies in each group. For the case of A400-a and A400-d, the

TABLE 7

TWO-BODY MODEL PARAMETERS

System (1)	M_{sys} ($10^{13}\ h^{-1}\ M_\odot$) (2)	$V_r \pm \Delta V_r$ (km s^{-1}) (3)	R_p (h^{-1} Mpc) (4)	Soln (5)	α (deg) (6)	V (km s^{-1}) (7)	R (h^{-1} Mpc) (8)	R_{max} (h^{-1} Mpc) (9)	Prob (10)
A400 ADL/ADH	24.9	1199 ± 87	0.31	BI_a	69.9	1276	0.90	2.87	0.54
				BI_b	32.1	2256	0.37	2.81	0.39
				BO	...	...	...	...	...
				UO	88.7	1199	13.5	...	0.07
A400 a/d	9.7	663 ± 89	0.16	BI_a	80.7	672	0.99	2.15	0.55
				BI_b	18.1	2132	0.17	2.04	0.40
				BO	...	...	...	...	...
				UO	88.9	663	7.98	...	0.05

derived separation is quite close to that obtained from the X-ray surface brightness fits described above. Column (5) lists the solution for which dynamical parameters are obtained, either BI_a or BI_b, the two possible bound and presently incoming solutions; BO, the bound and presently outgoing solution; or UO, the unbound outgoing solution. Columns (6)–(9) list the derived projected angle α, space velocity difference V, spatial separation R, and spatial separation at turnaround R_{max}, respectively. Column (10) lists quantitative estimates of the probability for each solution, obtained following the procedure of BGH.

Figure 19 is the two-body solution diagram for the A400-ADL + A400-ADH system, assuming that the total system mass is given by M'_v(A400-ADL) + M'_v(A400-ADH). At V_r = 1199 km s^{-1} both bound and unbound solutions exist. The system is bound and presently incoming with probability 93%. The bound incoming solution BI_a is marginally favored over the BI_b solution.

Figure 20 is the two-body solution diagram for the A400-a + A400-d system, assuming that the total system mass is given by M'_v(A400-a) + M'_v(A400-d). At V_r = 663 km s^{-1} both bound and unbound solutions exist. The system is bound and presently incoming with probability 94%. The bound incoming solution BI_a is marginally favored over the BI_b solution. Can we meaningfully choose between these solutions? As seen in Table 7, the solution BI_a corresponds to a projection angle of approximately 80° with respect to the plane of the sky, i.e., nearly along the line of sight. The inferred spatial velocity difference between the two subclusters is virtually identical to the measured radial velocity difference. The inferred spatial separation between the subclusters is roughly 1 Mpc, small enough that it would be difficult to verify with currrently available techniques for distance measurement. The solution BI_b corresponds to a projection angle of roughly 20° with respect to the plane of the sky. If this case pertains to A400, the subclusters are moving with relative spatial velocity difference on the order of 2000 km

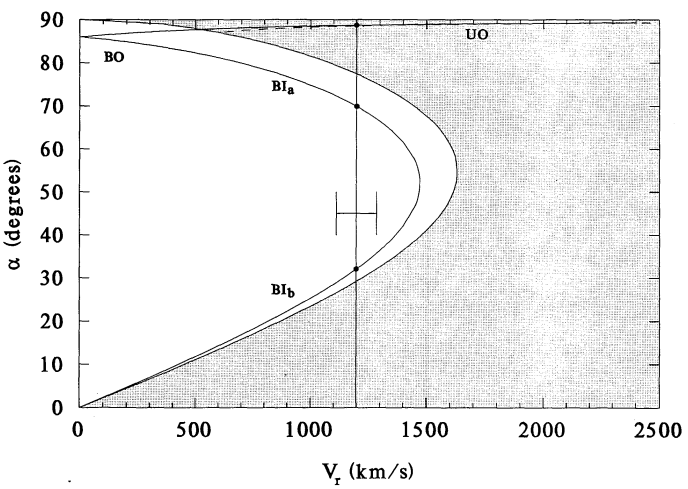

FIG. 19.—Projection angle α as a function of the radial velocity difference between the subclusters A400-ADL and A400-ADH given by the BGH two-body analysis for $t_0 = 3.1 \times 10^{17}\ h^{-1}$ s and $M_{sys} = 24.9 \times 10^{13}\ h\ M_\odot$. The regions of the bound incoming solutions BI_a and BI_b, the bound outgoing solutions BO, and the unbound outgoing solutions UO are indicated. The stippled area represents the unbound region. Hubble flow solutions approached in the limit of large V_r are indicated by the dashed line. The vertical solid line indicates the observed velocity difference between the subclusters at V_r = 1199 km s^{-1}. The filled circles represent the allowed solutions if the systemic radial velocity difference is set to this value. The error bar on the velocity line indicates the 68% limit in the observed radial velocity difference (ΔV_r = 87 km s^{-1}).

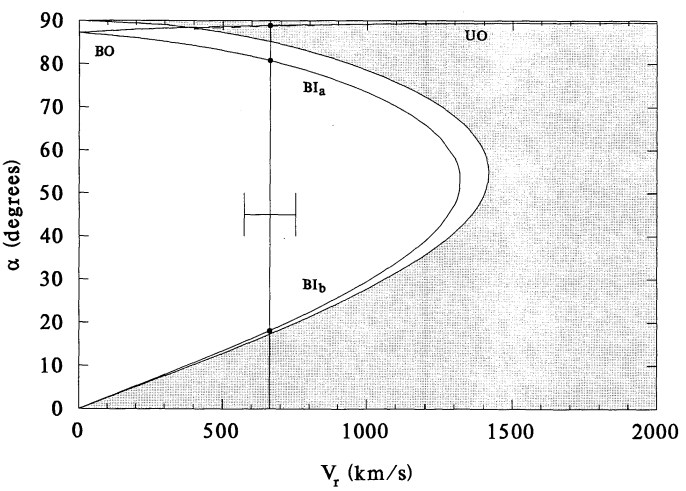

FIG. 20.—Projection angle α as a function of the radial velocity difference between the subclusters A400-a and A400-d given by the BGH two-body analysis for $t_0 = 3.1 \times 10^{17}\ h^{-1}$ s and $M_{sys} = 9.7 \times 10^{13}\ h\ M_\odot$. The regions of the bound incoming solutions BI_a and BI_b, the bound outgoing solutions BO, and the unbound outgoing solutions UO are indicated. The stippled area represents the unbound region. Hubble flow solutions approached in the limit of large V_r are indicated by the dashed line. The vertical solid line indicates the observed velocity difference between the subclusters at V_r = 663 km s^{-1}. The filled circles represent the allowed solutions if the systemic radial velocity difference is set to this value. The error bar on the velocity line indicates the 68% limit in the observed radial velocity difference (ΔV_r = 89 km s^{-1}).

s^{-1}, and are presently separated by no more than a few hundred kiloparsecs. Although the simple assumptions of the BGH analysis are expected to break down at the point where collision of the subclusters is imminent (see comments following Cavaliere & Colafrancesco 1990), this may be the preferable solution for A400, as discussed below.

6. SUMMARY AND DISCUSSION

We have argued that our extensive optical and X-ray data for A400 suggest a model in which the cluster is presently undergoing a merger of two primary subclusters of similar mass, although more complex merger scenarios cannot be ruled out. Direct evidence in support of this assertion includes the following:

1. The spatial distributions and kinematic properties of the elliptical and spiral subsamples can be clearly distinguished. The spiral galaxies populate the outer regions of the cluster and exhibit significant gaps in their radial velocity distribution.

2. A nearly complete redshift survey of the galaxies contained on the Dressler (1980) plate of A400 shows that the velocity distribution is unlikely to be consistent with draws from a single Gaussian parent population. A robust partitioning scheme identifies at least four individual groups in velocity space, one of which is a background group at a velocity of 13,400 km s^{-1}. Of the three remaining groups, one is spiral-rich, is located at the high end of the velocity distribution of the main cluster, and has member galaxies which appear to avoid the central region of the cluster. The other groups, which we identify as A400-a and A400-d, are separated in radial velocity by roughly 700 km s^{-1}, are dominated by elliptical galaxies, and populate the inner regions of the cluster.

3. The map of galaxy number density, when constructed exclusively from members of A400-a and A400-d, is a good match to the X-ray surface brightness map of A400. The secondary density peak seen in the galaxy map of Geller & Beers (1982) is shown to be due to the presence of galaxies from A400-b (the background group) and the group of dispersed spirals A400-c.

4. The dynamical masses inferred for the subclusters A400-a and A400-d are similar to the mass required to bind the X-ray–emitting gas. The derived dynamical mass of A400-AD, when taken as a single kinematical entity, or as the systems A400-ADL (groups A400-a *and* A400-d) and A400-ADH (group A400-c), is several times larger. The mass-to-light ratios of A400-a and A400-d are reasonable for groups and clusters (300–350 $h\ M_{\odot}/L_{\odot}$), whereas those obtained for A400-ADL and A400-ADH are roughly 600–1000 $h\ M_{\odot}/L_{\odot}$.

5. The X-ray surface brightness map is clearly elliptical in appearance, and can be well described (though not uniquely) by a model including two centers of emission, offset from one another by the same distance as the derived separation of the subclusters A400-a and A400-d. The simulations of Evrard (1990) indicate that elliptical X-ray surface brightness distributions are expected as a result of momentum transfer which takes place during a collision of subclusters. Indeed, as emphasized by Cavalier et al. (1983), the diffuse intracluster medium (ICM) provides the best tracer of the general gravitational potential. Any apparent mismatch between the X-ray map and the optical map may be the result of the fast relaxation of the gas as compared with the galaxies in the individual subclusters.

6. We obtain a value of $\beta_{\rm spec}$ consistent with $\beta_{\rm imag}$ by adopting the velocity dispersion of A400-ADL, $S_{\rm BI} = 486$ km s^{-1}. This result suggests that the X-ray–emitting gas is responding to the gravitational well of the still-forming cluster. The dispersions of the subclusters A400-a and A400-d are smaller (on the order of 200–300 km s^{-1}), indicating that the merger process is still in an early stage.

The ongoing-merger hypothesis simultaneously explains a number of possibly related facts, including the following:

a) The existence of the bright central dumbbell galaxy. Tremaine (1990) has argued that the individual components of dumbbell galaxies are D or cD galaxies because they were once the dominant galaxies in premerger subclusters. The dumbbell configuration is long-lived because dynamical friction does not become important until the cores of the individual subclusters have begun to merge, and the mutual drag of the dumbbell components begins to dominate that due to the subcluster cores. The two-body analysis of A400 suggests that the merger is presently underway. If the two-body solution BI_b pertains to A400, the cores of A400-a and A400-d are intermingling, with a present spatial separation on the order of 200 h^{-1} kpc. It is interesting to note that the velocities of the components which make up the dumbbell, galaxy 47 ($cz_h = 6800 \pm 15$ km s^{-1}) and 48 ($cz_h = 7236 \pm 15$ km s^{-1}), are within 100 and 150 km s^{-1} of their assigned subclusters A400-d ($C_{\rm BI} = 6709^{+76}_{-158}$ km s^{-1}) and A4000a ($C_{\rm BI} = 7386^{+67}_{-33}$ km s^{-1}), respectively.

b) The nature of the bending in the multiple radio jet 3C 75 associated with the components of the central dumbbell galaxy. The symmetry axis of the initial bend of the two wide-angle–tail (WAT) radio jets in 3C 75 (see Fig. 2 of Owen et al. 1985) is oriented with a position angle of approximately 30°–40° (counterclockwise from north). Thus it is aligned with the elliptical isophotes obtained from fits to the X-ray surface brightness map of A400 (see Figs. 16 and 17). This observation is consistent with a recent (or ongoing) subcluster collision—the ICMs of the colliding subclusters interact with the radio jets, bending them parallel to the axis of the collision. This model was at first rejected by Owen et al. (1985) on the grounds that the central galaxy of a cluster is not expected to obtain speeds relative to the cluster ICM that are sufficiently high (on the order of 1000 km s^{-1}) to bend the radio jets. As shown in the present paper, the high relative speed of the D galaxies which make up the dumbbell may be the result of the systematic motions of their subclusters.

The connection between cluster collapse and radio source morphology was suggested a decade ago by Sparke (1983), who noticed the greater incidence of distorted radio structures associated with the central galaxies of apparently clumpy or low X-ray temperature clusters. Also, it has been noted that the WAT sources are anticorrelated with the existence of a cooling flow in the X-rays. A400 shows no sign of cooling flow activity, either from the lack of a central excess of X-ray emission (Jones & Forman 1984) or from detailed modeling of the cooling time, for which Edge & Stewart (1991a) obtain $t_{\rm cool} = 19 \pm 25$ Gyr. A400 thus provides some support for the notion that cooling flow can be disrupted by subcluster collisions.

Additional observations are required to be certain of our ongoing-collision model for A400. Maps of the galaxy distribution based on catalogs which extend several magnitudes fainter than that of Dressler (1980) may resolve the cores of the individual subclusters A400-a and A400-d. If these subclusters are presently merging, the corresponding two-body model solution (BI_b) indicates a rather shallow inclination of the system

with respect to the line of sight (on the order of 20°). Thus we might expect that deeper X-ray maps of A400 (readily obtainable with *ROSAT*) may reveal the presence of a relatively sharp linear feature at low flux levels along a direction perpendicular to the collision axis, as is seen in A2256 (Briel et al. 1991) and in the collision models of Evrard (1990). Additional radial velocity measurements, particularly for faint elliptical galaxies in the central region of A400, should be obtained to verify the bimodal kinematic structure which we associated with A400-a and A400-d.

The authors would like to thank John Stauffer for kindly donating three velocities. T. C. B. is thankful to Margaret Geller for conversations concerning the nature of A400 at an early stage in this project. T. C. B. would like to express gratitude to Geoffrey McLachlan for kindly sending his mixture model code. T. C. B. and G. D. B. acknowledge partial support of this work from Bantrell Postdoctoral Fellowships at Caltech. G. D. B. also acknowledges partial support for a postdoctoral fellowship at the Center for Astrophysics. W. F. and C. J. acknowledge partial support from NASA contracts NAS 8-30751 and NASA 8-39073. J. P. H. acknowledges partial support from NASA grant NAGW-201 and the Smithsonian Institution.

REFERENCES

Aaronson, M., Bothun, G., Mould, J., Huchra, J., Schommer, R. A., & Cornell, M. E. 1986, ApJ, 302, 536
Abell, G. O. 1958, ApJS, 31, 211
Abt, H. A., & Biggs, E. S. 1972, Bibliography of Stellar Radial Velocities (Tucson: Kitt Peak National Observatory)
Beers, T. C., Flynn, K., & Gebhardt, K. 1990, AJ, 100, 32
Beers, T. C., Forman, W., Huchra, J. P., Jones, C., & Gebhardt, K. 1991, AJ, 102, 1581
Beers, T. C., Geller, M. J., & Huchra, J. P. 1982, ApJ, 257, 23 (BGH)
Bothun, G. D. 1981, Ph.D. thesis, Univ. Washington
Bothun, G. D., Aaronson, M., Schommer, R., Mould, J., Huchra, J. P., & Sullivan, W. T. 1985, ApJS, 57, 423
Briel, U. G., et al. 1991, A&A, 246, L10
Cavaliere, A., & Colafrancesco, S. 1990, in STScI Symp., Vol. 4, Clusters of Galaxies, ed. W. R. Oegerle, M. J. Fitchett, & L. Danly (Cambridge: Cambridge Univ. Press), 43
Cavaliere, A., deBiase, G. A., Sanangelo, O., & Vittorio, N. 1983, in Clustering in the Universe, ed. D. Gerbal & A. Mazure (Gif sur Yvette: Editions Frontières), 15
Cavaliere, A., & Fusco-Femiano, R. 1976, A&A, 49, 137
David, L. P., Arnaud, K. A., Forman, W., & Jones, C. 1990, ApJ, 356, 32
David, L. 1980, ApJS, 42, 565
Edge, A. C., & Stewart, G. C. 1991a, MNRAS, 252, 414
———. 1991b, MNRAS, 252, 428
Evrard, A. E. 1990, in STScI Symp., Vol. 4, Clusters of Galaxies, ed. W. R. Oegerle, M. J. Fitchett, & L. Danly (Cambridge: Cambridge Univ. Press), 287
Faber, S. M., & Gallagher, J. S. 1979, ARA&A, 17, 135
Fabricant, D., Lecar, M., & Gorenstein, P. 1980, ApJ, 241, 552
Gebhardt, K., & Beers, T. C. 1991, ApJ, 383, 72
Geller, M. J., & Beers, T. C. 1982, PASP, 94, 421
Hartigan, J. A., & Hartigan, P. M. 1985, Ann. Statistics, 13, 70
Haynes, M., & Giovanelli, R. 1984, AJ, 89, 758
Heisler, J., Tremaine, S., & Bahcall, J. N. 1985, ApJ, 298, 8
Henricksen, M. J., & Mushotzky, R. 1985, ApJ, 292, 441
Hintzen, P., Hill, J. M., Lindley, D., Scott, J. S., & Angel, J. R. P. 1982, AJ, 87, 1656
Hoaglin, D. C. 1985, in Exploring Data Tables, Trends, & Shapes, ed. D. C. Hoaglin, F. Mosteller, & J. W. Tukey (New York: Wiley), 417
Hoessel, J. G., Borne, K., & Schneider, D. P. 1985, ApJ, 293, 94
Huchra, J. P. 1990, private communication on redshift catalog sources
———. 1991, private communication
Jones, C., & Forman, W. 1984, ApJ, 276, 38
———. 1992, in preparation
Jones, C., Hughes, J., Stern, C., & Forman, W. 1992, private communication
Kaufman, L., & Rousseeuw, P. J. 1990, Finding Groups in Data: An Introduction to Cluster Analysis (New York: Wiley)
Latham, D. W. 1982, in IAU Colloq. 67, Instrumentation for Astronomy with Large Optical Telescopes, ed. C. M. Humphries (Dordrecht: Reidel), 259
Lauer, T. R. 1988, ApJ, 325, 49
McLachlan, G. J., & Basford, K. E. 1988, Mixture Models (New York: Dekker)
Nilson, P. 1973, Uppsala General Catalogue of Galaxies (Uppsala Astron. Obs. Ann., Vol. 6)
Owen, F. N., O'Dea, C. P., Inque, M., & Eilek, J. A. 1985, ApJ, 294, L85
Roeder, K. 1991, Inst. Math. Stat. Bull, 20, 273
Shectman, S. A., 1984, in Instrumentation in Astronomy V, ed. A. Boksenberg & D. L. Crawford (Proc. SPIE, Vol. 445), 128
Silverman, B. W. 1986, Density Estimation for Statistics and Data Analysis, (London: Chapman & Hall)
Sparke, L. S. 1983, Astrophys. Lett., 23, 113
Tonry, J. L. 1985, AJ, 90, 2431
Tonry, J. L., & Davis, M. 1979, AJ, 84, 1511
Tremaine, S. 1990, in Dynamics and Interactions of Galaxies, ed. R. Wielen (Berlin: Springer-Verlag), 394
Wanier, H., & Schacht, S. 1978, Psychometrika, 43, 203
West, M. J., & Bothun, G. D. 1990, ApJ, 350, 36
Wolfe, J. H. 1971, Tech. Bull. STB 72-2 (San Diego: US Naval Personel & Training Res. Lab.)
Zabludoff, A. I., Huchra, J. P., & Geller, M. J. 1990, ApJS, 74, 1
Zwicky, F., Herzog, E., Wild, P. Karpowicz, M., & Kowal, C. 1961–1968, Catalogue of Galaxies and Clusters of Galaxies (Pasadena: CIT)